Efficient and stable perovskite solar cells with a high open-circuit voltage over 1.2 V achieved by a dual-side passivation layer

Ju-Hyeon Kim[1,8†], Yong Ryun Kim[2†], Juae Kim[3], Chang-Mok Oh[4], In-Wook Hwang[4], Jehan Kim[5], Stefan Zeiske[2], Taeyoon Ki[1,8], Sooncheol Kwon[6], Heejoo Kim[7,8], Ardalan Armin[2], Hongsuk Suh[3*], Kwanghee Lee[1,8*]*

J-H. Kim, T. Ki, Prof. K. Lee
School of Materials Science and Engineering
Gwangju Institute of Science and Technology (GIST)
Gwangju 61005, Republic of Korea
E-mail: klee@gist.ac.kr

Y. Kim, S. Zeiske, A. Armin
Sustainable Advanced Materials (Sêr-SAM)
Department of Physics, Swansea University
Singleton Park, Swansea SA2 8PP, United Kingdom

J. Kim, Prof. H. Suh
Department of Chemistry and Chemistry Institute for Functional Materials
Pusan National University (PNU)
Busan 46241, Republic of Korea
E-mail: hssuh@pusan.ac.kr

C-M. Oh, I-W. Hwang
Advanced Photonics Research Institute
Gwangju Institute of Science and Technology (GIST)
Gwangju 61005, Republic of Korea

J. Kim
Pohang Accelerator Laboratory
Pohang University of Science and Technology
Pohang 37673, Republic of Korea

Prof. S. Kwon
Department of Energy and Materials Engineering
Dongguk University
Seoul 04620, Republic of Korea

Prof. H. Kim
Graduate School of Energy Convergence, Institute of Integrated Technology
Gwangju Institute of Science and Technology (GIST)
Gwangju 61005, Republic of Korea
E-mail: heejook@gist.ac.kr

J-H. Kim, T. Ki, Prof. H. Kim, Prof. K. Lee
Heeger Center for Advanced Materials (HCAM) and Research Institute for Solar and Sustainable Energies (RISE)
Gwangju Institute of Science and Technology (GIST)
Gwangju 61005, Republic of Korea
E-mail: heejook@gist.ac.kr, klee@gist.ac.kr

Keywords: organometal halide perovskite, perovskite solar cell, nonconjugated polymer, interface engineering, nonradiative recombination

Abstract

Suppressing nonradiative recombination at the interface between the organometal halide perovskite (PVK) and the charge transport layer (CTL) is crucial for improving the efficiency and stability of PVK-based solar cells (PSCs). Here, we synthesized a new bathocuproine (BCP)-based nonconjugated polyelectrolyte (poly-BCP) and introduced this as a 'dual-side passivation layer' between the tin oxide (SnO_2) CTL and the PVK absorber. Poly-BCP significantly suppressed both bulk and interfacial nonradiative recombination by passivating oxygen-vacancy defects from the SnO_2 side and simultaneously scavenging ionic defects from the other (PVK) side. Therefore, PSCs with poly-BCP exhibited a high power conversion efficiency (PCE) of 24.4% and a high open-circuit voltage of 1.21 V with a reduced voltage loss (PVK bandgap of 1.56 eV). The nonencapsulated PSCs also showed excellent long-term stability by retaining 93% of the initial PCE after 700 hours under continuous 1-sun irradiation in nitrogen atmosphere conditions.

1. Introduction

The recent rapid increase in power conversion efficiency (PCE) in organometal halide perovskite solar cells (PSCs) is attributed to the superior properties of perovskite (PVK) materials, such as high crystallinity, a long electron-hole diffusion length, and broad-range absorption.[1-4] Further improvement in PCE can be expected by reducing nonradiative recombination in PSCs, which is induced either by trap sites in the PVK layer or by minority carriers at the interface between the PVK layer and the charge transport layer (CTL).[5-12] Therefore, to minimize the nonradiative recombination loss in PSCs, maintaining high-quality PVKs and a clean interface between the CTL and the PVK layer is essential.[13-15]

The planar configuration is an emerging architecture for the future commercialization of PSCs due to its several advantages, such as less hysteresis, a lower processing temperature (≤150 °C), and much easier fabrication compared to mesoporous-type PSCs.[16-18] In particular, the minimized interfacial area in planar PSCs with a flattened CTL minimizes nonradiative recombination loss at the PVK/CTL interface.[13] Tin oxide (SnO_2) is widely used as an electron transport layer (ETL) in planar-type n-i-p PSCs due to its high electron mobility, excellent UV stability, and favorable conduction band edge for facilitating electron transfer from PVK.[19-25] However, the current PCE of SnO_2-based PSCs is still limited by the surface defects in SnO_2, especially oxygen vacancies.[26] They hinder efficient charge carrier extraction at the SnO_2/PVK interface, thereby leading to charge accumulation, and have a detrimental influence on subsequent PVK crystal growth.[27-29] This insufficient crystal growth also results in an increase in bulk defects at the grain boundaries of the PVK crystals. As a result, the combination of surface and bulk defects (from both the interface and PVK crystals) reduces the short-circuit current (J_{SC}) and open-circuit voltage (V_{OC}), resulting in a lower PCE in SnO_2-based PSCs.[30-33]

Passivating surface defects in SnO_2 has been achieved by several strategies, such as metallic ion doping[34-36], molecular coordination[26, 37-39], ligand tailoring[40, 41], and small

molecule anchoring[42-44] on the SnO_2 layer. Among them, solution-processed interlayers present a fascinating approach. By introducing π-conjugated small molecules[45-47] or self-assembled monolayers[48-50] with electron-donating functional groups (e.g., carbonyl, amine, and ammonium salt groups) between the SnO_2 and PVK layers, one can effectively passivate oxygen vacancies of SnO_2 through electrostatic interactions. However, the migration of small-molecule charged ions and the less-uniform formation of the small-molecule film on SnO_2 hamper the subsequent grain growth of PVK crystals and thereby induce an instability problem in PSCs.[20, 51] Therefore, the development of a more rigid interlayer film to overcome these weaknesses is highly desired.

Polyelectrolytes are a class of materials representing an ideal passivation layer due to their capability to tailor the electronic structure of adjacent layers by forming an electric dipole layer (EDL), which is induced by the charged functional groups of polyelectrolytes.[51-55] The strong electric field produced by an EDL enables charge carriers to be extracted efficiently at the interface, thereby minimizing recombination loss in PSCs.[56-58] Furthermore, due to the presence of electron-donating functional groups in polyelectrolytes, it is possible to passivate oxygen vacancies from the surface of SnO_2 and to scavenge cation defects from the PVK side at the same time.

In this work, we demonstrated highly efficient and stable PSCs by introducing a nonconjugated polyelectrolyte as an interfacial material at the SnO_2 ETL/PVK interface in an n-i-p planar structure. Our new bathocuproine (BCP)-core-based nonconjugated polyelectrolyte, poly[N-(6-phenyl)-1,10-phenanthrolin-4-yl]phenoxy}hexyl)-N,N-dimethylheptan-1-aminium bromide] (hereafter denoted as "poly-BCP"), passivates oxygen vacancies from the SnO_2 surface side and passivates PVK from the other side with enlarged PVK grains in the z-direction. As a result, the nonradiative recombination of PSCs is dramatically reduced, resulting in a significant increase in both V_{OC} (from 1.14 to 1.21 V) and J_{SC} (from 23.80 to 25.20 $mA \cdot cm^{-2}$). Therefore, the optimal cell with poly-BCP exhibited a high PCE of 24.4% (22.2% for the

control device). More importantly, nonencapsulated PSCs with poly-BCP exhibit excellent operating stability under continuous 1-sun irradiation in nitrogen atmosphere conditions over 700 hours (maintaining approximately 93% of the initial PCE).

2. Results and discussion

Figure 1a presents the chemical structure of poly-BCP used in this work, which was confirmed by ^{1}H-nuclear magnetic resonance (H-NMR) spectroscopy (Figure S1), and the detailed synthesis route is described in supplementary scheme 1. The BCP molecule was chosen as a core molecule because of its high electron affinity, which enhances charge carrier transport and extraction ability at the SnO_2/PVK interface.[45] The quaternary ammonium bromide ($NR_4^+Br^-$) functional group is attached to the BCP molecule to effectively passivate interfacial defects and induce the electrical dipole moment to minimize the energy loss at the SnO_2/PVK interface.[59] Finally, an alkyl chain bridge is introduced to enhance solubility and maintain the characteristics of the BCP molecule.

The excellence of our approach lies in the design strategy of the chemical structure for this poly-BCP. The polymerization in poly-BCP is achieved through alkyl chain bridges (and is therefore nonconjugated), in contrast with the conventional polymerization methods connecting BCP molecules (which are conjugated). Therefore, our poly-BCP conserves the molecular nature of BCP without sacrificing its excellent transport characteristics but still reinforces the uniform distribution of BCP molecules throughout the layer without any aggregation.

To confirm the possibility of EDL formation in poly-BCP, we initially simulated the electrostatic potential (ESP) of poly-BCP. As shown in Figure 1b and supplementary scheme 2, we observed a high charge distribution at both nitrogen atoms in the BCP core and the $NR_4^+Br^-$ functional group, suggesting that poly-BCP can passivate the oxygen vacancies of SnO_2 or cationic defects in PVK. Furthermore, due to the excellent thermal stability of poly-

BCP (see Figure S2, thermal decomposition is observed at 260 °C), poly-BCP preserves its own characteristics at the PVK phase transition temperature (≤150 °C). The electronic structure of poly-BCP was explored by UV–Vis absorption spectroscopy incorporating cyclic voltammetry (CV) measurements (see Figures S3 and S4). The UV–Vis absorption spectrum of the poly-BCP film exhibits a vibronic structure similar to that of the BCP molecule, as we expect in our poly-BCP design strategy (the details are summarized in Table S1). In addition, the wide transparency in the visible range of poly-BCP indicates that this material is suitable for the interfacial layer located at the bottom of the PVK film without any optical loss, as shown in Figure 1c.

To clarify the effect of poly-BCP as an EDL on SnO_2, we conducted ultraviolet photoelectron spectroscopy (UPS) analysis on two samples: i) SnO_2 and ii) SnO_2/poly-BCP. As shown in Figure 1d, the work function (WF) of SnO_2 changed from 4.17 eV to 3.97 eV after introducing the poly-BCP layer. This result was also cross-checked by performing Kelvin probe measurements (Figure S5). Furthermore, Kelvin probe force microscopy (KPFM, Figure S6) analysis reveals that the surface potential is uniformly increased throughout the film and that the variation in surface potential is reduced by introducing poly-BCP onto indium tin oxide (ITO) or SnO_2 substrates. Therefore, as shown in Figure 1e, a reduction in the energetic disorder between SnO_2 and PVK is expected.

To examine the surface passivation role of poly-BCP on SnO_2, we performed high-resolution X-ray photoelectron spectroscopy (HR-XPS) on the SnO_2 and SnO_2/poly-BCP films. Figure S7 (a) shows that the two distinct peaks of Sn $3d_{3/2}$ (494.78 eV) and Sn $3d_{5/2}$ (486.38 eV) in the SnO_2 film are shifted toward lower binding energies of 494.58 and 486.18 eV in the SnO_2/poly-BCP film, respectively, implying that a change is made in the chemical environment of Sn.[60] It indicates a decreased valence state of the Sn atoms by interacting with poly-BCP.[28, 61] Besides, in Figure S7 (b), the poly-BCP film reveals two peaks of Br $3d_{3/2}$ (68.3 eV) and Br $3d_{5/2}$ (67.2 eV). However, in the SnO_2/poly-BCP film, these peaks are shifted toward slightly

higher binding energies, and an additional peak at 69.2 eV is observed, which is assigned to Sn-Br binding energy[62] due to electrostatic coupling from the functional group in poly-BCP. Moreover, the deconvoluted HR-XPS spectra of O1s for the SnO_2 film in Figure S7 (c) can be resolved into two oxygen states (530.3 eV and 531.3 eV), while three oxygen states (530.3 eV, 531.2 eV and 532.6 eV) are obtained for the SnO_2/poly-BCP film, which are assigned to the Sn-O-Sn lattice binding energy (O_L), oxygen-related vacancies (O_V) and oxygen in poly-BCP (O_P), respectively.[26, 51] Based on these spectra, we calculated the peak area ratio of O_v/O_{ALL}, where O_{ALL} is the whole area of the O1s spectrum. As summarized in Table S2, the peak ratio of the SnO_2 film decreases from 0.44 to 0.20 in the SnO_2/poly-BCP film, indicating that the O_v on the surface of SnO_2 is effectively suppressed by the bromide ion in poly-BCP via electrostatic coupling, thus confirming the passivation effect of poly-BCP on the O_v of SnO_2.

The different crystal growth of the PVK films on SnO_2 and SnO_2/poly-BCP was explored by scanning electron microscopy (SEM) measurements. As shown in Figure S8, the PVK film on SnO_2/poly-BCP shows enlarged grain features, corresponding to a reduction in the number of grain boundaries and voids compared to those of the control PVK film on SnO_2. This observation is also confirmed by the atomic force microscopy (AFM) images depicted in Figure S8, in which the root mean square of the PVK films is effectively reduced from 36.62 nm (control) to 30.31 nm (modified poly-BCP). To acquire information on the crystallinity of the PVK film, we conducted X-ray diffraction (XRD) analysis on the PVK films deposited on SnO_2 and SnO_2/poly-BCP (Figure S9). Although the XRD patterns for the two films are similar, a noticeable change is observed for two peaks at 12.6° and 14.2°, which are attributed to the (001) diffraction peak of hexagonal PbI_2 and the (110) plane of the PVK film, respectively.[63] The PVK film on the SnO_2/poly-BCP samples shows a decreased intensity of the (001) peak of PbI_2 and an increased intensity of the (110) peak of PVK compared to the control PVK films on SnO_2. These results indicate that poly-BCP leads to better PVK grain growth. For more detailed information on the crystal growth of the PVK film, we conducted 2D grazing-incidence

wide-angle X-ray scattering (GIWAXS) measurements of the PVK films on SnO_2 (**Figure 2**a) and SnO_2/poly-BCP (Figure 2b). Two strong diffraction patterns appear at $q_{x,y}$ = 1.0 $Å^{-1}$ and 2.0 $Å^{-1}$ for both PVK films, which correspond to the (110) and (220) planes of the PVK film, respectively.[64] Furthermore, the 1D scattering profiles (Figure S10) show that the PVK films on both underlying layers have a preference for the out-of-plane direction. However, the PVK film on SnO_2/poly-BCP shows a higher intensity of the (220) plane (Figure 2b), which indicates a higher crystallinity and higher z-directional orientation compared to the PVK film on SnO_2 (Figure 2c).[65-67] Therefore, we infer that poly-BCP promotes higher-quality PVK films during subsequent PVK film deposition.

Our assumption is confirmed by the steady-state photoluminescence (PL) and time-resolved PL (TRPL) results for the poly-BCP/PVK and control PVK films, which were all prepared on quartz glass substrates. A twofold increase in PL intensity was observed in poly-BCP/PVK compared to the control PVK film (Figure 2d), indicating a reduction in nonradiative recombination at the bulk PVK material. The TRPL results in Figure 2e were fitted with a biexponential function (the detailed decay profiles are summarized in **Table 1**). The fast decay component (τ_1) is assigned to nonradiative recombination induced by charge carriers trapping defect states, whereas the slow decay component (τ_2) is related to bimolecular radiative recombination in the bulk PVK material.[33, 68] Note that when employing poly-BCP on PVK, the decay time and the proportion of τ_1 decrease (from 19.3 ns to 17.6 ns and from 46% to 25%), while the proportion of τ_2 increases (from 54% to 75%). As a result, a longer average charge carrier lifetime (τ_{avg}) was observed in the poly-BCP/PVK films (from 79.1 ns to 103.2 ns). Therefore, these results indicate that the higher z-directional orientation of the PVK film with an enlarged grain size on the poly-BCP layer effectively reduces nonradiative recombination in the PVK film.

PSCs were fabricated with a planar n-i-p structure of ITO/SnO_2 without or with poly-BCP/$(CsPbI_3)_{0.05}[(FAPbI_3)_{0.97}(MAPbBr_3)_{0.03}]_{0.95}$ based on PVK/spiro-OMeTAD/Au. **Figure 3**a

shows the cross-sectional SEM image of the PSC with poly-BCP. Figure S11 shows the PV performances of PSCs with different concentrations of poly-BCP; and the best performance was obtained with 1.0 mg/ml poly-BCP in methanol, which corresponds to a poly-BCP film thickness of 7 nm on SnO_2 (Figure S12). The current-voltage (*J-V*) characteristics of the optimized PSCs without or with poly-BCP are presented in Figure 3b. As summarized in **Table 2**, the PSCs with poly-BCP exhibited a V_{OC} of 1.21 V, a J_{SC} of 25.21 mA·cm^{-2}, and a fill factor (FF) of 80.12%, yielding a PCE of 24.43%. These values are substantially higher than those of the control devices (a V_{OC} of 1.14 V, a J_{SC} of 23.86 mA·cm^{-2}, an FF of 80.75 % and a PCE of 22.22%). The measured J_{SC} values agree well with the integrated J_{SC} values calculated from the incident photon-to-current efficiency (IPCE) spectra (Figure 3c). Note that the PSCs with poly-BCP have a relatively high V_{OC} value compared to previous reports, which recorded PCEs over 24% (Figure 3d and Table S3). Furthermore, in the statistics for the distribution of V_{OC} and J_{SC}, the PSCs with poly-BCP exhibited a narrower distribution (see Figure 3e), attributed to the enlarged grain boundaries with smoother surface morphology observed in the SEM and AFM results. Therefore, the reproducibility and accuracy of PCEs were improved, as shown in the PCE histogram for the PSCs (Figure 3f).

According to the Shockley-Queisser limit theory, the V_{OC} loss of solar cells is the sum of the radiative loss above bandgap ($\Delta V_{OC,SC}$), radiative loss below bandgap ($\Delta V_{OC,Rad}$) and nonradiative loss ($\Delta V_{OC,Nonrad}$).[69, 70] To calculate the loss in radiative and nonradiative recombination, we measured the bandgap of PVK films and the electroluminescence external quantum efficiency (EQE_{EL}) of the PSCs.[71] As shown in Figure S13, the PVK films with and without poly-BCP exhibited similar bandgaps, implying the same $\Delta V_{OC,SC}$ value for the two devices. However, a threefold increase in the EQE_{EL} of PSC after introducing poly-BCP (from 2.7% to 9.9%, **Figure 4**a) indicates a dramatic reduction in the calculated $\Delta V_{OC,Nonrad}$ from 93 mV to 59 mV (see Figure S14), respectively, as shown in Figure S14. In addition, detailed balance analyses were conducted on both devices, where the non-radiative voltage losses, as

obtained from the EQE_{PV} spectra (Figure 4b), were calculated to ~70 mV (w/poly BCP) and ~127 mV (as control) device (the details are summarized in Figure S15). These values are in good agreement with non-radiative voltage losses determined from EQE_{EL}. Therefore, the high V_{OC} obtained in PSCs with poly-BCP is partially attributed to a dramatic suppression of nonradiative recombination in the PSCs. To confirm the reduced $\Delta V_{OC,Nonrad}$, we investigated the charge dynamics in the PSCs by transient photovoltage (TPV) measurements under open-circuit conditions. As shown in Figure 4c and **Table 3**, the average decay times of the photovoltage of PSCs with poly-BCP are much longer (465.9 μs) than those of the control devices (135 μs), indicating that poly-BCP effectively suppresses the nonradiative recombination of PSCs. This conclusion agrees well with the light-intensity (P_{light}) dependence of the V_{OC} of PSCs. As shown in Figure 4d, the slopes of the curves were calculated to be 1.39 kT/q (control devices) and 1.03 kT/q (w/poly-BCP), wherein k, T, and q are the Boltzmann constant, Kelvin temperature, and elementary charge constant, respectively. This result also supports that trap-assisted charge recombination is effectively suppressed in the PSCs with poly-BCP.

Further insight into the exciton dissociation and charge extraction properties of the PSCs with poly-BCP is obtained from the photogenerated current density (J_{PH}) versus effective voltage (V_{eff}) characteristics of the PSCs (Figure S16). After introducing poly-BCP, the generation values at the maximum power point (G_{MPP}) and short-circuit condition (G_{SC}) are increased. We attribute the enhanced G values and V_{oc} of PSCs with poly-BCP to a reduced trap density of the PVK film with poly-BCP. To quantify the bulk trap density in PVK films, space-charge limited current (SCLC) measurements were conducted on electron-only devices (ITO/ETL without or with poly-BCP/PVK/C60/Al). As shown in Figure 4e (control) and f (w/poly-BCP), the calculated trap density for the control device is approximately 3.53×10^{15} cm^{-2}, while a reduced trap density (1.82×10^{15} cm^{-2}) is obtained in the poly-BCP devices. Therefore, the enhanced PV performance of the PSCs with poly-BCP is attributed to the

enhanced charge carrier dissociation in PVK materials and charge carrier collection toward each electrode.

To investigate the charge transport at the ETL/PVK interface, we performed TRPL measurements on PVK films with different ETLs (SnO_2 and SnO_2/poly-BCP). In addition, transient photocurrent (TPC) measurements and impedance spectroscopy (IS) for PSCs with different ETLs were performed. As shown in Figure S17 and Table S4, the τ_{avg} of the PVK film on SnO_2/poly-BCP (18.6 ns) is much shorter than that of the control PVK film on SnO_2 (27.2 ns), indicating that the charge carrier transport at the SnO_2/PVK interface increases when poly-BCP is employed. This result agrees well with the steady-state PL measurements (inset of Figure S17). Accordingly, as shown in Figure S18 and Table 3, the TPC measurements on the PSCs also showed a decreased decay time from 0.68 μs (control) to 0.39 μs (w/poly-BCP), indicating enhanced charge carrier extraction at the PVK/ETL interface. The Nyquist plots obtained from IS also showed a significant decrease in the charge transport resistance from 6.23 x 10^3 Ω to 1.69 x 10^3 Ω after introducing poly-BCP between the PVK film and SnO_2 (see Figure S19 and Table S5).[72] Consequently, the reduced trap density of the PVK film with poly-BCP also affects charge extraction at the ETL/PVK interface.

We further investigated the electronic structure of PVK films on different ETLs. **Figure 5**a and b show KPFM images of PVK films on SnO_2 and SnO_2/poly-BCP, respectively. The corresponding surface line profiles (Figure 5c) for each sample show that the average contact potential difference values of the PVK film on SnO_2/poly-BCP (~360 mV) are lower than those of the PVK film on SnO_2 (~410 mV). These results are well matched with the UPS results (Figure S20 and S21). The WF of the PVK material with poly-BCP exhibits more p-type-like properties. The calculated difference in WF (corresponding to the built-in-potential, V_{bi}) at the ETL/PVK interface (Table S6, Figure 5d and e) shows that SnO_2/poly-BCP/PVK exhibited a larger V_{bi} of 0.330 eV than that (0.001 eV) of the SnO_2/PVK film. These results indicate that the incorporation of poly-BCP suppressed the nonradiative recombination induced

by both trap-assisted recombinations at the bulk PVK absorber and minority carrier recombination at the ETL/PVK interface.[56, 73-77] Finally, we examined the photostability (maximum power point tracking stability) of nonencapsulated PSCs under continuous photoillumination (AM 1.5G, 100 $mW \cdot cm^{-2}$) in a nitrogen atmosphere. As shown in Figure 5f, the PSCs with poly-BCP have higher operational stability; after 750 hours of exposure, the PSC with poly-BCP exhibited 7% degradation relative to the initial efficiency, whereas a 17% degradation from the initial efficiency was observed in the control device. Therefore, this result confirms that the passivation function of poly-BCP effectively enhances the stability of PSCs under harsher conditions.

3. Conclusion

In conclusion, we successfully demonstrated highly efficient and stable planar configuration n-i-p PSCs employing poly-BCP as a double-side passivation layer between the SnO_2 ETL and the PVK layer. Poly-BCP induces enhanced crystallinity along the vertical growth direction with an enlarged grain size. In addition, it effectively passivates oxygen vacancies in both SnO_2 and PVK defects and enhances charge carrier transportability through reinforced built-in potential on the ETL/PVK interface. As a result, the planar PSCs show high PCE values of 24.4% with an enhanced V_{OC} of 1.21 V, indicating minimized nonradiative voltage loss. Furthermore, nonencapsulated PSCs with poly-BCP exhibit better operation stability than the control devices, maintaining almost ~93% of their initial performance for more than 700 h under continuous 1-sun irradiation in nitrogen atmosphere conditions. We are confident that our approach will offer a new direction for demonstrating both highly efficient PSCs and PVK-based optoelectronic applications.

4. Experimental

4.1. Materials

For the electron transport layer (ETL) solution, the SnO_2 colloid precursor (tin(IV) oxide, 15% in H_2O colloidal dispersion) was purchased from Alfa Aesar and diluted with deionized water (1:5 volume ratio). Lead(II) iodide (PbI_2), lead(II) bromide ($PbBr_2$), and cesium iodide (CsI) were purchased from TCI, and phenethylammonium iodide (PEAI, $C_8H_{12}IN$), formamidinium iodide (FAI, CH_5IN_2), and methylammonium bromide (MABr, CH_6BrN) were purchased from Great Cell Solar and were used without any pretreatment. The 1.5 M triple-cation-based PVK precursor solution, $(CsPbI_3)_{0.05}[(FAPbI_3)_{0.97}(MAPbBr_3)_{0.03}]_{0.95}$ + 30 mol% methylammonium chloride (MACl, Merck KGaA), was prepared by dissolution in anhydrous N,N-dimethylformamide (DMF)/dimethyl sulfoxide (DMSO) mixed solution (4:1 volume ratio). The hole transport layer (HTL) 2,2′,7,7′-tetrakis(*N,N*-di-4-methoxyphenylamine)-9,9′-spirobifluorene (spiro-OMeTAD, Sigma–Aldrich) solution was dissolved in chlorobenzene at a concentration of 91 $mg \cdot mL^{-1}$. After that, 21.02 μL bis(trifluoromethane) sulfonimide lithium salt (Li-TFSI, Sigma–Aldrich) solution (520 $mg \cdot mL^{-1}$ in acetonitrile), 10 μL tris(2-(1*H*-pyrazol-1-yl)-4-*tert*-butylpyridine)-cobalt(III) tri[bis(trifluoromethane)sulfonimide] (FK209, Sigma–Aldrich) solution (375 $mg \cdot mL^{-1}$ in acetonitrile) and 35.65 μL 4-tert-butylpyridine (Sigma–Aldrich) were added to the spiro-OMeTAD solution.

4.2. Polymer synthesis

Synthesis of poly-BCP: 4,7-bis[4-(6-(*N*,*N*-Dimethylamino-hexyloxy)phenyl]-2,9-dimethyl-1,10-phenanthroline (0.1 g, 0.1546 mmol) and 1,6-dibromohexane (0.02 ml, 0.1546 mmol) in 3 ml of 2,2,2-trifluoroethanol were stirred at RT until all reagents were dissolved. After Na_2CO_3 (0.033 g, 0.3138 mmol) was added to the reaction mixture, the mixture was heated at 70 °C for 2 days. After the reaction finished, the reaction mixture was precipitated into hexane, filtered, and washed with hexane. Then, the product was obtained as a pure light yellow solid (0.4 g, 27%) and characterized by ^{1}H NMR and GPC (M_n = 10.2 kDa). ^{1}H NMR (300 MHz, $CDCl_3$): δ (ppm) 7.756 (s, 1H) 7.460-7.380 (m, 3H) 7.017 (d, 2H, J = 8.8 Hz) 4.601-

4.250 (m, 2H) 4.076 (t, 2H, J = 5.8 Hz) 3.620-3.500 (m, 4H) 3.480-3.400 (m, 2H) 3.423 (s, 6H) 3.380-3.200 (m, 4H) 2.971 (s, 3H) 1.850-1.250 (m, 22H).

4.3. Device fabrication

n-i-p planar PSCs were fabricated with the structure ITO/SnO_2 without or with poly-BCP/perovskite (PVK)/spiro-OMeTAD/Au. The SnO_2 ETL layer was spin-coated onto UV-ozone-treated patterned ITO substrates at a spin speed of 3000 rpm for 30 s with annealing at 150 °C for 30 min. Then, the substrates were transferred into a N_2-filled glove box. The poly-BCP solution in methanol was coated on a SnO_2 substrate at 3000 rpm for 30 s. The PVK layer was fabricated by two consecutive spin-coating steps at 1000 rpm and 5000 rpm for 5 s and 20 s, respectively; 800 μL of diethyl ether was quickly dropped as an antisolvent after 5 s of the second spin step and then annealed at 150 °C for 10 min. After the PVK film was cooled, a large iodide cation solution (OAI or PEAI, 1 mg/ml in IPA) was spin-coated on the PVK film at 3000 rpm for 30 s for top surface passivation without thermal annealing.[78] Afterward, the fabricated HTL, doped spiro-OMeTAD solution, was spin-coated at 3000 rpm for 30 s. Finally, an 80 nm gold (Au) top electrode was deposited via the thermal evaporation process under high vacuum conditions at an evaporation rate of 0.01 nm/s.

4.4. Material characterization

$^{1}H/^{13}C$ NMR spectra were recorded on a Varian Gemini-300 spectrometer. DSC analysis was performed on a DSC Q200 at a heating rate of 10 °C/min from room temperature to 300 °C (heating-cooling-heating-cooling). Thermogravimetric analysis (TGA) was performed with an SDT Q600 instrument in a nitrogen atmosphere at a heating rate of 10 °C/min to 600 °C. Electrochemical CV measurements were conducted using a Wona-WPG100 (Austin, Texas, USA).

4.5. Thin-film characterization

The UV–Vis-NIR absorption spectra were collected by a UV–Vis-NIR spectrophotometer. (Cary 5000 UV–Vis-NIR, Agilent Technologies, Inc.). The steady-state PL

spectra were measured by a fluorescence spectrophotometer (Hitachi F-4500, Hitachi, Ltd.). The high-resolution XRD profiles were collected by SmartLab (Rigaku, Japan). XPS and UPS spectra were obtained using a NEXSA (Thermo Fisher Scientific, USA) instrument with an Al–Kα X-ray source and He (I) (21.22 eV) UV source, respectively. Ultrahigh-resolution FESEM was performed with a Verios 5 UC (Thermo Fisher Scientific, USA) under high vacuum conditions. AFM and KPFM images were obtained using an XE-100 (Park System, Korea) microscope and Multimode 8 (Bruker, USA) with a Pt/Ir-coated Si probe (Bruker, SCM-PIT-V2, USA) at + 0.5 V applied DC bias, respectively. The GIWAXS measurements were performed at the 3C-WAXSl beamline in the Pohang Accelerator Laboratory using a monochromatized X-ray radiation source of 10.55 eV (λ = 1.170 Å) and a 2D charge-coupled detector (CCD) (model Rayonix 2D SX 165, Rayonix, Evanston, IL, USA). The values of the work function (WF) were obtained using a KP 6500 digital Kelvin probe (McAllister Technical Services, Co.). For film thickness measurements, ellipsometry measurements were conducted by an M-2000 (J.A. Woollam Co., Inc) under incident angles of 60, 65 and 70°. The film was deposited on a silicon substrate to avoid the interference of surface reflection. The molecular geometry of the monomer and the ESP analysis of the monomer and polymer were optimized by ADF with the B3LYP-D functional and the TZP basis set.

4.5. Theoretical studies of simulated poly-BCP

In our density functional theory (DFT) study, we employed Becke's three-parameter hybrid method and the Lee-Yang-Parr correlation functional (B3LYP)[79, 80] using the Amsterdam Density Functional (ADF) program.[81] We calculated the geometry optimization and electrostatic surface potential distribution of poly-BCP with a Slater-type TZ2P basis set for H, C, O, N, and Br atoms.[82]

4.6. Device characterization

The time-resolved fluorescence-decay profile, transient photocurrent (TPC), and voltage (TPV) were recorded using an oscilloscope (Waverunner 625Zi, Teledyne LECROY)

coupled with a 470 nm picosecond laser (P-C-470, PicoQuant GmbH) as the excitation source. The decay time constants for the fluorescence-decay profiles were obtained by first deconvoluting the pump time profile (characterized by a full width at half maximum of ≈70 ps) and then fitting the results to a sum of exponential terms. To measure TPC and TPV, we changed the input impedance of the oscilloscope to 50 Ω and 1 MΩ, respectively, and exposed the samples to an excitation pulse laser with a repetition rate of 50 Hz to 100 kHz. TPC and TPV were determined from the average of over 20,000 measurements for each sample.

The current density-voltage (*J-V)* characteristics of the devices were measured under AM 1.5G illumination with an irradiation intensity of 100 mW cm^{-2} using a solar simulator (Sol 3A, Newport Corp) and a source/meter unit (Keithley 2420, Keithley Instruments, Inc.), which was calibrated using a certified reference standard silicon solar cell (Newport Corp.). The incident-photon-to-electron conversion efficiency (IPCE) measurements were performed by using a quantum efficiency measurement system (Quant X-300, Newport Corp.) with a chopping frequency of 100 Hz, which was calibrated by using a 603621 calibrated reference detector (Newport Corp.). Impedance spectroscopy was conducted using a PGSTAT30 (Metrohm Autolab B.V., Netherlands) in a frequency range between 0.1 and 1 MHz under dark conditions. Sensitive external quantum efficiency (EQE) measurements were conducted using a commercial UV/VIS/NIR spectrophotometer (Perkin Elmer, Lambda950) as a light source. The monochromator output light was physically chopped (Thorlabs, MC2000B) at 273 Hz. The device under test (DUT) was mounted into an electrically shielded sample holder (Linkam) under purging with dry nitrogen. The photocurrent of the DUT was fed into a low-noise current preamplifier (FEMTO, DLPCA-200) before the signal was detected with a lock-in amplifier (Stanford Research Systems, SR860) at an electrical bandwidth of 1/300 Hz. For the EQE calibration process, a NIST-calibrated silicon (Si) photodiode sensor from Newport (818-UV) was used. Detailed information on the experimental setup is provided elsewhere.[83] The EQE_{EL}

characteristics were measured using a PR650 spectrophotometer with a Keithley 2400 source measure unit.

Supporting Information

Supporting Information is available from the Online Library or from the author.

Acknowledgments

J.-H. K. and Y. K. contributed equally to this work. J.-H. K. thanks the Heeger Center for Advanced Materials (HCAM) at the Gwangju Institute of Science and Technology (GIST) for the assistance with device fabrication and analysis. This work was supported by the Global Research Laboratory (GRL) Program of the National Research Foundation (NRF) of Korea funded by the Ministry of Science, ICT & Future Planning (MSIP) (NRF-2017K1A1A2013153); by the Technology Development Program to Solve Climate Change of the NRF funded by MSIT (NRF-2020M1A2A2080748); by the program of Future Hydrogen Original Technology Development (No. 2021M313A1084747) through the NRF funded by MSIT; by the Basic Science Research Program through the NRF funded by the Ministry of Education (2020R1I1A3061306), (2022R1A6A3A13055321); and by the GIST Research Institute (GRI, RISE) via a grant funded by the GIST in 2022.

Received: ((will be filled in by the editorial staff))
Revised: ((will be filled in by the editorial staff))
Published online: ((will be filled in by the editorial staff))

References

[1] G. Xing, N. Mathews, S. Sun, S. Lim Swee, M. Lam Yeng, M. Grätzel, S. Mhaisalkar, C. Sum Tze, Science 2013, 342, 344.

[2] D. Stranks Samuel, E. Eperon Giles, G. Grancini, C. Menelaou, J. P. Alcocer Marcelo,

T. Leijtens, M. Herz Laura, A. Petrozza, J. Snaith Henry, Science 2013, 342, 341.

[3] M. I. Saidaminov, K. Williams, M. Wei, A. Johnston, R. Quintero-Bermudez, M. Vafaie, J. M. Pina, A. H. Proppe, Y. Hou, G. Walters, S. O. Kelley, W. A. Tisdale, E. H. Sargent, Nature Materials 2020, 19, 412.

[4] S.-H. Turren-Cruz, A. Hagfeldt, M. Saliba, Science 2018, 362, 449.

[5] S. Mahesh, J. M. Ball, R. D. J. Oliver, D. P. McMeekin, P. K. Nayak, M. B. Johnston, H. J. Snaith, Energy & Environmental Science 2020, 13, 258.

[6] M. Daboczi, I. Hamilton, S. Xu, J. Luke, S. Limbu, J. Lee, M. A. McLachlan, K. Lee, J. R. Durrant, I. D. Baikie, J.-S. Kim, ACS Applied Materials & Interfaces 2019, 11, 46808.

[7] C.-T. Lin, J. Lee, J. Kim, T. J. Macdonald, J. Ngiam, B. Xu, M. Daboczi, W. Xu, S. Pont, B. Park, H. Kang, J.-S. Kim, D. J. Payne, K. Lee, J. R. Durrant, M. A. McLachlan, Advanced Functional Materials 2020, 30, 1906763.

[8] M. Stolterfoht, C. M. Wolff, J. A. Márquez, S. Zhang, C. J. Hages, D. Rothhardt, S. Albrecht, P. L. Burn, P. Meredith, T. Unold, D. Neher, Nature Energy 2018, 3, 847.

[9] M. Stolterfoht, P. Caprioglio, C. M. Wolff, J. A. Márquez, J. Nordmann, S. Zhang, D. Rothhardt, U. Hörmann, Y. Amir, A. Redinger, L. Kegelmann, F. Zu, S. Albrecht, N. Koch, T. Kirchartz, M. Saliba, T. Unold, D. Neher, Energy & Environmental Science 2019, 12, 2778.

[10] C. M. Wolff, P. Caprioglio, M. Stolterfoht, D. Neher, Advanced Materials 2019, 31, 1902762.

[11] I. Levine, A. Al-Ashouri, A. Musiienko, H. Hempel, A. Magomedov, A. Drevilkauskaite, V. Getautis, D. Menzel, K. Hinrichs, T. Unold, S. Albrecht, T. Dittrich, Joule 2021, 5, 2915.

[12] J. Shi, Y. Li, Y. Li, D. Li, Y. Luo, H. Wu, Q. Meng, Joule 2018, 2, 879.

[13] H. Min, D. Y. Lee, J. Kim, G. Kim, K. S. Lee, J. Kim, M. J. Paik, Y. K. Kim, K. S. Kim, M. G. Kim, T. J. Shin, S. Il Seok, Nature 2021, 598, 444.

[14] W. Yang, H. Long, X. Sha, J. Sun, Y. Zhao, C. Guo, X. Peng, C. Shou, X. Yang, J. Sheng, Z. Yang, B. Yan, J. Ye, Advanced Functional Materials 2022, 32, 2110698.

[15] J.-P. Correa-Baena, Y. Luo, M. Brenner Thomas, J. Snaider, S. Sun, X. Li, A. Jensen Mallory, P. Hartono Noor Titan, L. Nienhaus, S. Wieghold, R. Poindexter Jeremy, S. Wang, S. Meng Ying, T. Wang, B. Lai, V. Holt Martin, Z. Cai, G. Bawendi Moungi, L. Huang, T. Buonassisi, P. Fenning David, Science 2019, 363, 627.

[16] D. Liu, T. L. Kelly, Nature Photonics 2014, 8, 133.

[17] F. Liu, J. Zhu, J. Wei, Y. Li, M. Lv, S. Yang, B. Zhang, J. Yao, S. Dai, Applied Physics

Letters 2014, 104, 253508.

[18] H. Yoon, S. M. Kang, J.-K. Lee, M. Choi, Energy & Environmental Science 2016, 9, 2262.

[19] Q. Jiang, L. Zhang, H. Wang, X. Yang, J. Meng, H. Liu, Z. Yin, J. Wu, X. Zhang, J. You, Nature Energy 2016, 2, 16177.

[20] T. Bu, J. Li, F. Zheng, W. Chen, X. Wen, Z. Ku, Y. Peng, J. Zhong, Y.-B. Cheng, F. Huang, Nature Communications 2018, 9, 4609.

[21] T. Bu, S. Shi, J. Li, Y. Liu, J. Shi, L. Chen, X. Liu, J. Qiu, Z. Ku, Y. Peng, J. Zhong, Y.-B. Cheng, F. Huang, ACS Applied Materials & Interfaces 2018, 10, 14922.

[22] H. J. Snaith, C. Ducati, Nano Letters 2010, 10, 1259.

[23] W. Ke, G. Fang, Q. Liu, L. Xiong, P. Qin, H. Tao, J. Wang, H. Lei, B. Li, J. Wan, G. Yang, Y. Yan, Journal of the American Chemical Society 2015, 137, 6730.

[24] S. S. Shin, W. S. Yang, J. H. Noh, J. H. Suk, N. J. Jeon, J. H. Park, J. S. Kim, W. M. Seong, S. I. Seok, Nature Communications 2015, 6, 7410.

[25] J. P. Correa Baena, L. Steier, W. Tress, M. Saliba, S. Neutzner, T. Matsui, F. Giordano, T. J. Jacobsson, A. R. Srimath Kandada, S. M. Zakeeruddin, A. Petrozza, A. Abate, M. K. Nazeeruddin, M. Grätzel, A. Hagfeldt, Energy & Environmental Science 2015, 8, 2928.

[26] B. Parida, I. S. Jin, J. W. Jung, Chemistry of Materials 2021, 33, 5850.

[27] X. Shi, R. Chen, T. Jiang, S. Ma, X. Liu, Y. Ding, M. Cai, J. Wu, S. Dai, Solar RRL 2020, 4, 1900198.

[28] Z. Xiong, L. Lan, Y. Wang, C. Lu, S. Qin, S. Chen, L. Zhou, C. Zhu, S. Li, L. Meng, K. Sun, Y. Li, ACS Energy Letters 2021, 6, 3824.

[29] X. Liu, Y. Zhang, L. Shi, Z. Liu, J. Huang, J. S. Yun, Y. Zeng, A. Pu, K. Sun, Z. Hameiri, J. A. Stride, J. Seidel, M. A. Green, X. Hao, Advanced Energy Materials 2018, 8, 1800138.

[30] D. Luo, W. Yang, Z. Wang, A. Sadhanala, Q. Hu, R. Su, R. Shivanna, F. Trindade Gustavo, F. Watts John, Z. Xu, T. Liu, K. Chen, F. Ye, P. Wu, L. Zhao, J. Wu, Y. Tu, Y. Zhang, X. Yang, W. Zhang, H. Friend Richard, Q. Gong, J. Snaith Henry, R. Zhu, Science 2018, 360, 1442.

[31] X. Zheng, J. Troughton, N. Gasparini, Y. Lin, M. Wei, Y. Hou, J. Liu, K. Song, Z. Chen, C. Yang, B. Turedi, A. Y. Alsalloum, J. Pan, J. Chen, A. A. Zhumekenov, T. D. Anthopoulos, Y. Han, D. Baran, O. F. Mohammed, E. H. Sargent, O. M. Bakr, Joule 2019, 3, 1963.

[32] Z. Wang, Q. Lin, F. P. Chmiel, N. Sakai, L. M. Herz, H. J. Snaith, Nature Energy 2017, 2, 17135.

[33] T.-H. Han, J.-W. Lee, C. Choi, S. Tan, C. Lee, Y. Zhao, Z. Dai, N. De Marco, S.-J. Lee, S.-H. Bae, Y. Yuan, H. M. Lee, Y. Huang, Y. Yang, Nature Communications 2019, 10, 520.

[34] M. Park, J.-Y. Kim, H. J. Son, C.-H. Lee, S. S. Jang, M. J. Ko, Nano Energy 2016, 26, 208.

[35] J. Tian, J. Zhang, X. Li, B. Cheng, J. Yu, W. Ho, Solar RRL 2020, 4, 2000090.

[36] Y. W. Noh, J. H. Lee, I. S. Jin, S. H. Park, J. W. Jung, Nano Energy 2019, 65, 104014.

[37] Y. Ge, F. Ye, M. Xiao, H. Wang, C. Wang, J. Liang, X. Hu, H. Guan, H. Cui, W. Ke, C. Tao, G. Fang, Advanced Energy Materials 2022, n/a, 2200361.

[38] P. Wang, B. Chen, R. Li, S. Wang, N. Ren, Y. Li, S. Mazumdar, B. Shi, Y. Zhao, X. Zhang, ACS Energy Letters 2021, 6, 2121.

[39] H. Gao, X. Wei, R. Yu, F.-Y. Cao, Y. Gong, Z. Ma, Y.-J. Cheng, C.-S. Hsu, Z. a. Tan, Advanced Optical Materials 2022, 10, 2102031.

[40] Z. Ren, K. Liu, H. Hu, X. Guo, Y. Gao, P. W. K. Fong, Q. Liang, H. Tang, J. Huang, H. Zhang, M. Qin, L. Cui, H. T. Chandran, D. Shen, M.-F. Lo, A. Ng, C. Surya, M. Shao, C.-S. Lee, X. Lu, F. Laquai, Y. Zhu, G. Li, Light: Science & Applications 2021, 10, 239.

[41] J. Dong, J. Jia, X. Feng, B. Shi, Y. Wu, Y. Zhang, J. Wu, B. Cao, Journal of Alloys and Compounds 2021, 883, 160827.

[42] K. Choi, J. Lee, H. I. Kim, C. W. Park, G.-W. Kim, H. Choi, S. Park, S. A. Park, T. Park, Energy & Environmental Science 2018, 11, 3238.

[43] K. Liu, S. Chen, J. Wu, H. Zhang, M. Qin, X. Lu, Y. Tu, Q. Meng, X. Zhan, Energy & Environmental Science 2018, 11, 3463.

[44] Z. Wang, M. A. Kamarudin, N. C. Huey, F. Yang, M. Pandey, G. Kapil, T. Ma, S. Hayase, ChemSusChem 2018, 11, 3941.

[45] R. Chen, B. Long, S. Wang, Y. Liu, J. Bai, S. Huang, H. Li, X. Chen, ACS Applied Materials & Interfaces 2021, 13, 24747.

[46] J. Ge, L. Hong, W. Song, L. Xie, J. Zhang, Z. Chen, K. Yu, R. Peng, X. Zhang, Z. Ge, Advanced Energy Materials 2021, 11, 2100800.

[47] X. Zhao, L. Tao, H. Li, W. Huang, P. Sun, J. Liu, S. Liu, Q. Sun, Z. Cui, L. Sun, Y. Shen, Y. Yang, M. Wang, Nano Letters 2018, 18, 2442.

[48] Z. Dai, K. Yadavalli Srinivas, M. Chen, A. Abbaspourtamijani, Y. Qi, P. Padture Nitin, Science 2021, 372, 618.

[49] G. Tumen-Ulzii, T. Matsushima, D. Klotz, M. R. Leyden, P. Wang, C. Qin, J.-W. Lee, S.-J. Lee, Y. Yang, C. Adachi, Communications Materials 2020, 1, 31.

[50] M. Hou, H. Zhang, Z. Wang, Y. Xia, Y. Chen, W. Huang, ACS Applied Materials & Interfaces 2018, 10, 30607.

[51] Z. Xiong, X. Chen, B. Zhang, G. O. Odunmbaku, Z. Ou, B. Guo, K. Yang, Z. Kan, S. Lu, S. Chen, N. A. N. Ouedraogo, Y. Cho, C. Yang, J. Chen, K. Sun, Advanced Materials 2022, 34, 2106118.

[52] J. H. Kang, Y. J. Park, Y. Khan, Y. Ahn, J. H. Seo, B. Walker, Dyes and Pigments 2020, 182, 108634.

[53] P.-H. Liu, C.-H. Chuang, Y.-L. Zhou, S.-H. Wang, R.-J. Jeng, S.-P. Rwei, W.-B. Liau, L. Wang, Journal of Materials Chemistry A 2020, 8, 25173.

[54] L. Zhang, X. Zhou, J. Xie, S. Chen, S. Bae, J. Kim, B. Xu, Journal of Materials Chemistry A 2020, 8, 8238.

[55] H. Choi, C.-K. Mai, H.-B. Kim, J. Jeong, S. Song, G. C. Bazan, J. Y. Kim, A. J. Heeger, Nature Communications 2015, 6, 7348.

[56] J.-H. Lee, J. Kim, G. Kim, D. Shin, S. Y. Jeong, J. Lee, S. Hong, J. W. Choi, C.-L. Lee, H. Kim, Y. Yi, K. Lee, Energy & Environmental Science 2018, 11, 1742.

[57] H. Wang, Y. Song, Y. Kang, S. Dang, J. Feng, Q. Dong, Journal of Materials Chemistry A 2020, 8, 7309.

[58] X. Huang, J. Du, X. Guo, Z. Lin, J. Ma, J. Su, L. Feng, C. Zhang, J. Zhang, J. Chang, Y. Hao, Solar RRL 2020, 4, 1900336.

[59] X. Zheng, B. Chen, J. Dai, Y. Fang, Y. Bai, Y. Lin, H. Wei, Xiao C. Zeng, J. Huang, Nature Energy 2017, 2, 17102.

[60] M. Liao, B.-B. Yu, Z. Jin, W. Chen, Y. Zhu, X. Zhang, W. Yao, T. Duan, I. Djerdj, Z. He, ChemSusChem 2019, 12, 5007.

[61] N. Li, X. Niu, F. Pei, H. Liu, Y. Cao, Y. Liu, H. Xie, Y. Gao, Q. Chen, F. Mo, H. Zhou, Solar RRL 2020, 4, 1900217.

[62] E. L. Lee, A. S. M. A. Haseeb, W. J. Basirun, Y. H. Wong, M. F. M. Sabri, B. Y. Low, Scientific Reports 2021, 11, 15768.

[63] T. J. Jacobsson, J.-P. Correa-Baena, E. Halvani Anaraki, B. Philippe, S. D. Stranks, M. E. F. Bouduban, W. Tress, K. Schenk, J. Teuscher, J.-E. Moser, H. Rensmo, A. Hagfeldt, Journal of the American Chemical Society 2016, 138, 10331.

[64] J.-H. Kim, Y. R. Kim, B. Park, S. Hong, I.-W. Hwang, J. Kim, S. Kwon, G. Kim, H. Kim, K. Lee, Small 2021, 17, 2005608.

[65] M. Jahandar, N. Khan, M. Jahankhan, C. E. Song, H. K. Lee, S. K. Lee, W. S. Shin, J.-C. Lee, S. H. Im, S.-J. Moon, Data in Brief 2019, 27, 104817.

[66] G. Zheng, C. Zhu, J. Ma, X. Zhang, G. Tang, R. Li, Y. Chen, L. Li, J. Hu, J. Hong, Q. Chen, X. Gao, H. Zhou, Nature Communications 2018, 9, 2793.

[67] X. Zheng, Y. Hou, C. Bao, J. Yin, F. Yuan, Z. Huang, K. Song, J. Liu, J. Troughton, N. Gasparini, C. Zhou, Y. Lin, D.-J. Xue, B. Chen, A. K. Johnston, N. Wei, M. N. Hedhili, M. Wei, A. Y. Alsalloum, P. Maity, B. Turedi, C. Yang, D. Baran, T. D. Anthopoulos, Y. Han, Z.-H. Lu, O. F. Mohammed, F. Gao, E. H. Sargent, O. M. Bakr, Nature Energy 2020, 5, 131.

[68] Y.-W. Jang, S. Lee, K. M. Yeom, K. Jeong, K. Choi, M. Choi, J. H. Noh, Nature Energy 2021, 6, 63.

[69] J. Wang, J. Zhang, Y. Zhou, H. Liu, Q. Xue, X. Li, C.-C. Chueh, H.-L. Yip, Z. Zhu, A. K. Y. Jen, Nature Communications 2020, 11, 177.

[70] K. Vandewal, K. Tvingstedt, A. Gadisa, O. Inganäs, J. V. Manca, Physical Review B 2010, 81, 125204.

[71] H. Lu, Y. Liu, P. Ahlawat, A. Mishra, R. Tress Wolfgang, T. Eickemeyer Felix, Y. Yang, F. Fu, Z. Wang, E. Avalos Claudia, I. Carlsen Brian, A. Agarwalla, X. Zhang, X. Li, Y. Zhan, M. Zakeeruddin Shaik, L. Emsley, U. Rothlisberger, L. Zheng, A. Hagfeldt, M. Grätzel, Science 2020, 370, eabb8985.

[72] W. Xu, L. Zheng, X. Zhang, Y. Cao, T. Meng, D. Wu, L. Liu, W. Hu, X. Gong, Advanced Energy Materials 2018, 8, 1703178.

[73] N. K. Sinha, D. S. Ghosh, A. Khare, Optical Materials 2022, 129, 112517.

[74] C. Ahläng, M. Nyman, R. Österbacka, Physical Review Applied 2021, 16, 014041.

[75] S. Liu, S. Wu, P. Xia, H. Xie, X. Yuan, Y. Li, D. Kong, H. Huang, Y. Gao, C. Zhou, Applied Physics Letters 2022, 120, 253503.

[76] A. Mahapatra, N. Parikh, P. Kumar, M. Kumar, D. Prochowicz, A. Kalam, M. M. Tavakoli, P. Yadav, Molecules 2020, 25.

[77] J. Diekmann, P. Caprioglio, M. H. Futscher, V. M. Le Corre, S. Reichert, F. Jaiser, M. Arvind, L. P. Toro, E. Gutierrez-Partida, F. Peña-Camargo, C. Deibel, B. Ehrler, T. Unold, T. Kirchartz, D. Neher, M. Stolterfoht, Solar RRL 2021, 5, 2100219.

[78] Q. Jiang, Y. Zhao, X. Zhang, X. Yang, Y. Chen, Z. Chu, Q. Ye, X. Li, Z. Yin, J. You, Nature Photonics 2019, 13, 460.

[79] A. D. Becke, The Journal of Chemical Physics 1993, 98, 5648.

[80] C. Lee, W. Yang, R. G. Parr, Physical Review B 1988, 37, 785.

[81] G. te Velde, F. M. Bickelhaupt, E. J. Baerends, C. Fonseca Guerra, S. J. A. van Gisbergen, J. G. Snijders, T. Ziegler, Journal of Computational Chemistry 2001, 22, 931.

[82] E. Van Lenthe, E. J. Baerends, Journal of Computational Chemistry 2003, 24, 1142.

[83] S. Zeiske, C. Kaiser, P. Meredith, A. Armin, ACS Photonics 2020, 7, 256.

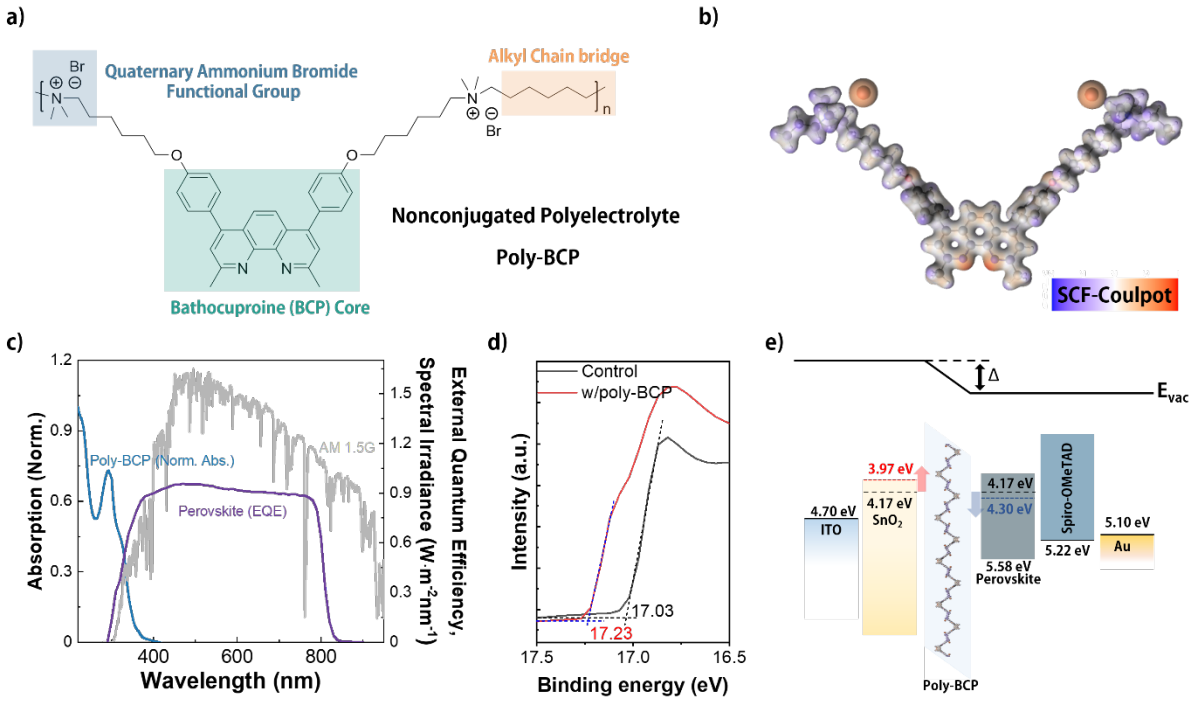

Figure 1. Electronic and optoelectronic characteristics. a) Chemical structure of poly-BCP. b) Molecular electrostatic potential (ESP) analysis of repeat units of poly-BCP. The inset image bar indicates the self-consistent field coulomb potential (SCF-Coulpot): negative (red) and positive (purple). c) UV–Vis absorption spectrum of poly-BCP (blue), the external quantum efficiency (EQE) of PSCs (purple) and the solar spectrum (gray). d) Secondary electron cutoff region of UPS data for the control SnO_2 film (black) and SnO_2/poly-BCP film (red). e) Energy level diagram for a planar n-i-p configuration of PSCs in open-circuit condition - corresponding change in work function of each material; SnO_2 (red) and perovskite (blue).

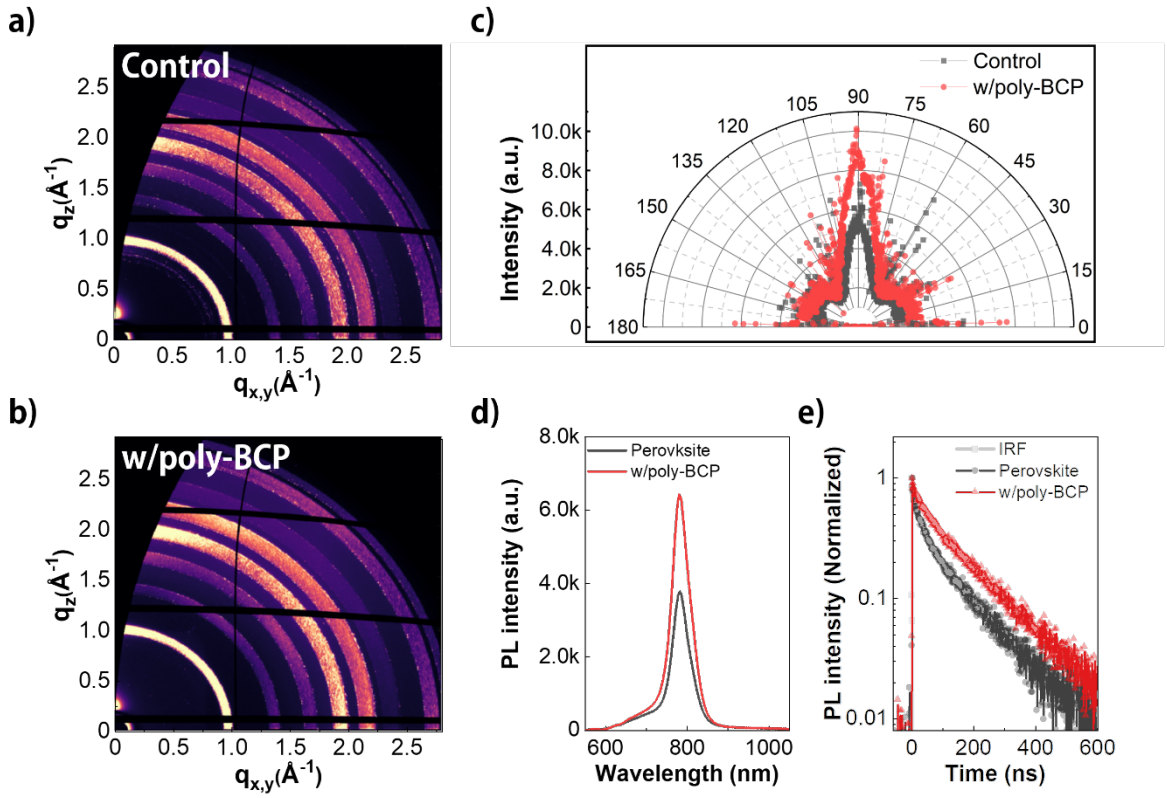

Figure 2. Characteristics of PVK thin film samples on SnO_2 (control) and SnO_2/poly-BCP (w/poly-BCP). 2D GIWAXS patterns of the PVK thin films: a) control and b) w/poly-BCP samples. c) 1D GIWAXS azimuthal plots of the corresponding PVK (110) plane: control (black) and w/poly-BCP (red) PVK films. d) Steady-state PL and e) TRPL decay curves of control (black) and w/poly-BCP (red) PVK thin films on a quartz glass substrate.

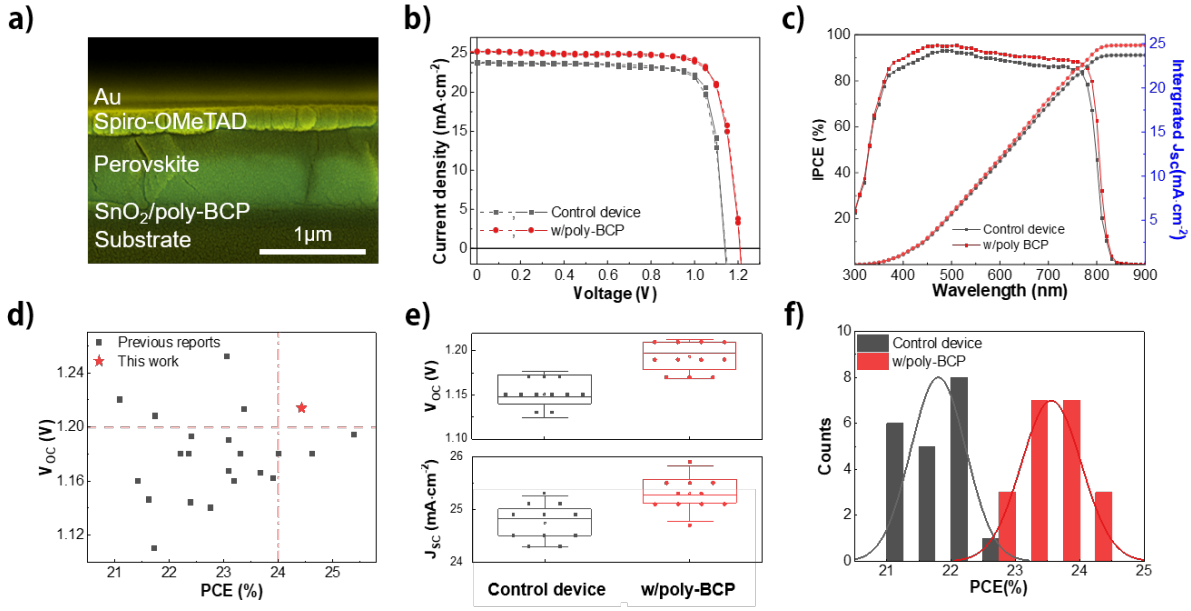

Figure 3. Device structure and PV performance of PSCs. a) Cross-sectional SEM image of PSCs with poly-BCP. b) Current density-voltage (J-V) curves of optimized devices in the forward (dotted line) and reverse (solid line) scan directions. c) EQE spectra and integrated J_{SC} values from EQE spectra of PSCs: control device (black) and w/poly-BCP device (red). d) Comparison of PSC performance with the V_{OC} of each device reported in the literature (in Table S3). e) Histogram of each PV parameter: V_{OC} (upper) and J_{SC} (lower). f) Distribution of PCEs for PSCs: control devices (black) and w/poly-BCP devices (red).

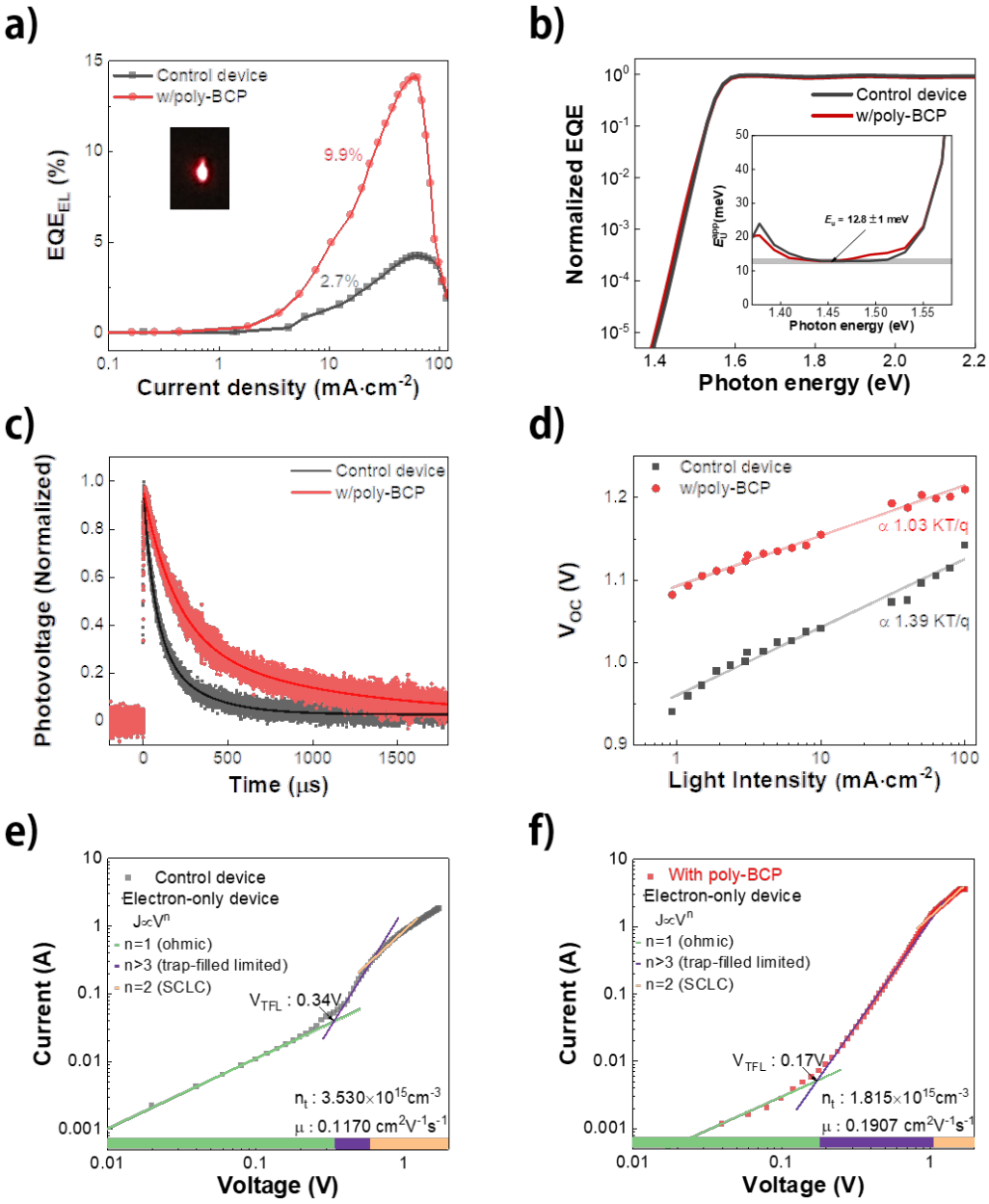

Figure 4. Trap state of PVK materials. a) EQE_{EL} versus current density plot of PSCs – an EL image of a PSC is shown in the inset. b) Normalized EQE of an as control (black) and w\poly-BCP (red) device plotted as a function of photon energy. The inset shows the corresponding apparent Urbach energy spectra, $\boldsymbol{E_U^{app}(E)}$, as calculated via $\boldsymbol{E_U^{app}(E) = \left[\frac{d\ln(EQE_{PV})}{dE}\right]^{-1}}$ (where $\boldsymbol{E}$ is the photon energy), plotted as a function of photon energy. An Urbach energy of $\boldsymbol{E_U = 12.8 \pm 1}$ meV was determined for both devices. c) TPV measurement of PSCs. d) Light intensity dependence of V_{OC}: control (black) and w/poly-BCP (red) devices. I-V characteristics of the electron-only device (ITO/SnO_2 with or without poly-BCP/PVK/C60/Al), e) control device (black) and f) w/poly-BCP device (red): the ohmic contact region (green), space-charge limited current region (beige), and trap-filled-limited region (purple). Corresponding electron mobility and trap density (inset).

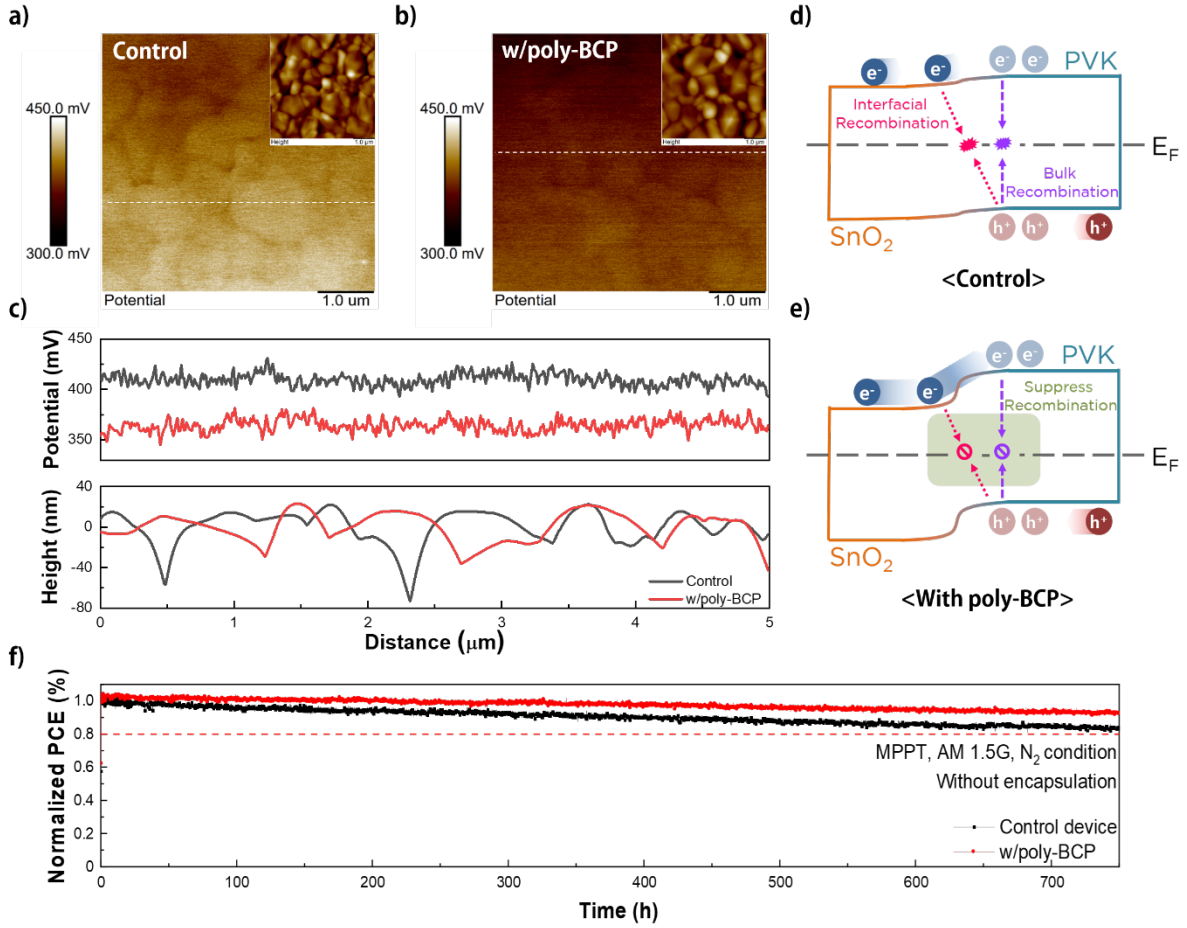

Figure 5. Charge transport of PVK materials. Kelvin probe force microscopy (KPFM) surface potential images of a PVK thin film on a) SnO_2 (control) and b) SnO_2/poly-BCP (w/poly-BCP); the AFM topology images are shown in the insets. The color scale bar of the KPFM images indicates the relative scale of the surface potential: bright regions indicate high potential, and dark regions indicate low potential. The white dotted lines across the images denote the locations used to extract the potential profiles in c); surface potential line profiles of the corresponding PVK films: control (black) and w/poly-BCP (red). Illustration of the charge transport process at the interface between SnO_2 and the PVK layer under short circuit conditions: d) control and e) w/poly-BCP. f) Maximum power point tracking (MPPT) of the PSCs under continuous AM 1.5G 1 sun illumination in N_2 without encapsulation: control device (black) and w/poly-BCP device (red).

Table 1. PL decay parameters of each sample.

Samples[a)]	Fitted time constants[b)] (ns)		
	τ_1	τ_2	τ_{avg} [c)]
Perovskite	19.3 (46%)	130.1 (54%)	79.1
Poly-BCP/perovskite	17.6 (25%)	131.8 (75%)	103.2

[a)] Excitation wavelengths of 470 nm (a repetition rate of 500 kHz and an intensity of 1.6 μW) and emission wavelengths of 790 nm were used; [b)] The decay curves were fitted using a biexponential decay model: $I(t) = A_1 \exp(-t/\tau_1) + A_2 \exp(-t/\tau_2)$, where $I(t)$: time-dependent fluorescence intensity, A: amplitude (noted in parentheses as the normalized percentage, i.e., $[A_i/(A_1 + A_2)] \times 100$), and τ: fitted decay time. [c)] τ_{avg}: average decay time. The χ^2 values for the deconvolution fitting are 0.99~1.1.

Table 2. Photovoltaic performance parameters of the PSCs.

Sample	*Sweep direction*	V_{OC} (V)	J_{SC} (mA·cm^{-2})	IPCE[a)] (mA·cm^{-2})	FF	PCE[b)] (%)	PCE[c)] (%)
Control device	Forward	1.14	23.75	23.70	80.61	21.94	21.78
	Reverse	1.14	23.86		80.75	22.22	21.82
w/poly-BCP	Forward	1.21	25.20	24.82	79.37	24.20	23.84
	Reverse	1.21	25.21		80.12	24.43	24.06

[a)] Calculated current density obtained by integrating the EQE spectrum; [b)] PCE from the J-V curve; [c)] PCE corrected by the current obtained through EQE.

Table 3. Decay time of TPV and TPC measurements of PSCs.

Samples	Fitted value [a)] (μs)		
	τ_1	τ_2	$\tau_{avg.}$
	TPV		
Control device	67.9 (64%)	255.3 (36%)	135
w/poly-BCP	190.4 (64%)	950.1 (36%)	465.9
	TPC		
Control device	0.06 (47%)	1.22 (53%)	0.68
w/poly-BCP	0.12 (77%)	1.28 (23%)	0.39

[a)] The decay curves are fitted using a biexponential decay model.

New synthesized non-conjugated polyelectrolyte is introduced as an interfacial layer between the charge transport layer and perovskite absorbent, which significantly reduce both bulk and interfacial nonradiative recombination losses, but also aligns the interfaces energy level. The champion device is a power conversion efficiency of 24.4% (open-circuit voltage 1.2V in perovskite band gap 1.56eV) with negligible hysteresis and superior operational stability.

Ju-Hyeon Kim[1,8†], Yong Ryun Kim[2†], Juae Kim[3], Chang-Mok Oh[4], In-Wook Hwang[4], Jehan Kim[5], Stefan Zeiske[2], Taeyoon Ki[1,8], Sooncheol Kwon[6], Heejoo Kim[7,8*], Ardalan Armin[2], Hongsuk Suh[3*], Kwanghee Lee[1,8*]

Efficient and stable perovskite solar cells with a high open-circuit voltage over 1.2 V achieved by a dual-side passivation layer

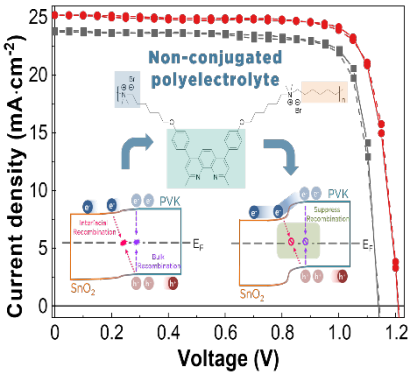

Supporting Information

Efficient and stable perovskite solar cells with a high open-circuit voltage over 1.2 V achieved by a dual-side passivation layer

Ju-Hyeon Kim[1,8†], Yong Ryun Kim[2†], Juae Kim[3], Chang-Mok Oh[4], In-Wook Hwang[4], Jehan Kim[5], Stefan Zeiske[2], Taeyoon Ki[1,8], Sooncheol Kwon[6], Heejoo Kim[7,8], Ardalan Armin[2], Hongsuk Suh[3*], Kwanghee Lee[1,8*]*

J-H. Kim, T. Ki, Prof. K. Lee
School of Materials Science and Engineering, Gwangju Institute of Science and Technology, Gwangju 61005, Republic of Korea
E-mail: klee@gist.ac.kr

Y. Kim, S. Zeiske, A. Armin
Sustainable Advanced Materials (Sêr-SAM), Department of Physics, Swansea University, Singleton Park, Swansea SA2 8PP, United Kingdom

J. Kim, Prof. H. Suh
Department of Chemistry and Chemistry Institute for Functional Materials, Pusan National University (PNU), Busan 46241, Republic of Korea
E-mail: hssuh@pusan.ac.kr

C-M. Oh, I-W. Hwang
Advanced Photonics Research Institute, Gwangju Institute of Science and Technology, Gwangju 61005, Republic of Korea

J. Kim
Pohang Accelerator Laboratory, Pohang University of Science and Technology, Pohang 37673, Republic of Korea

Prof. S. Kwon
Department of Energy and Materials Engineering, Dongguk University, Seoul 04620, Republic of Korea

Prof. H. Kim
Graduate School of Energy Convergence, Institute of Integrated Technology, Gwangju Institute of Science and Technology, Gwangju 61005, Republic of Korea
E-mail: heejook@gist.ac.kr

J-H. Kim, T. Ki, Prof. H. Kim, Prof. K. Lee
Heeger Center for Advanced Materials (HCAM) and Research Institute for Solar and Sustainable Energies (RISE), Gwangju Institute of Science and Technology, Gwangju 61005, Republic of Korea
E-mail: heejook@gist.ac.kr, klee@gist.ac.kr

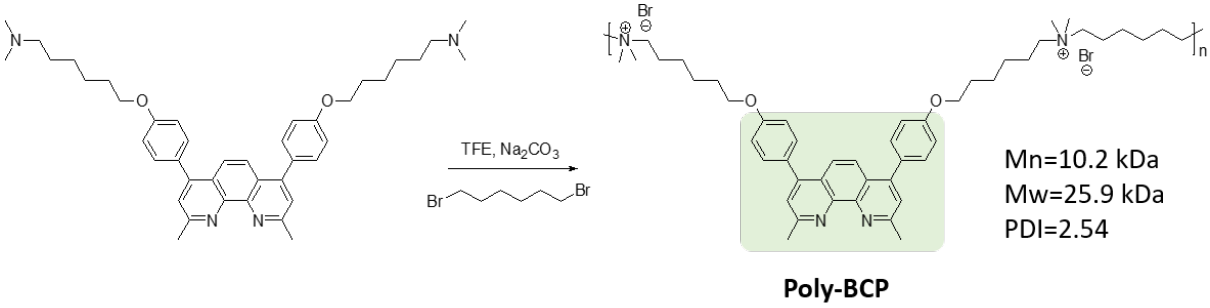

Scheme S1. Synthetic route of poly-BCP and its chemical structure.

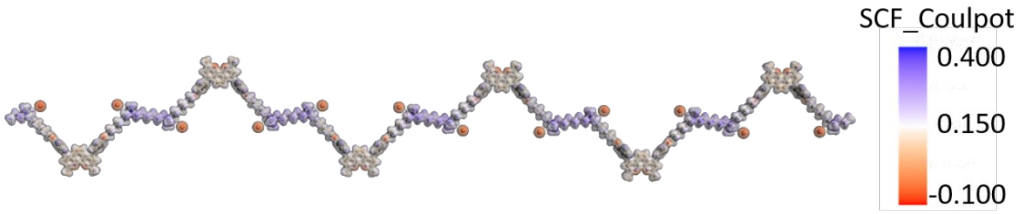

Scheme S2. Calculating electron density of poly-BCP.

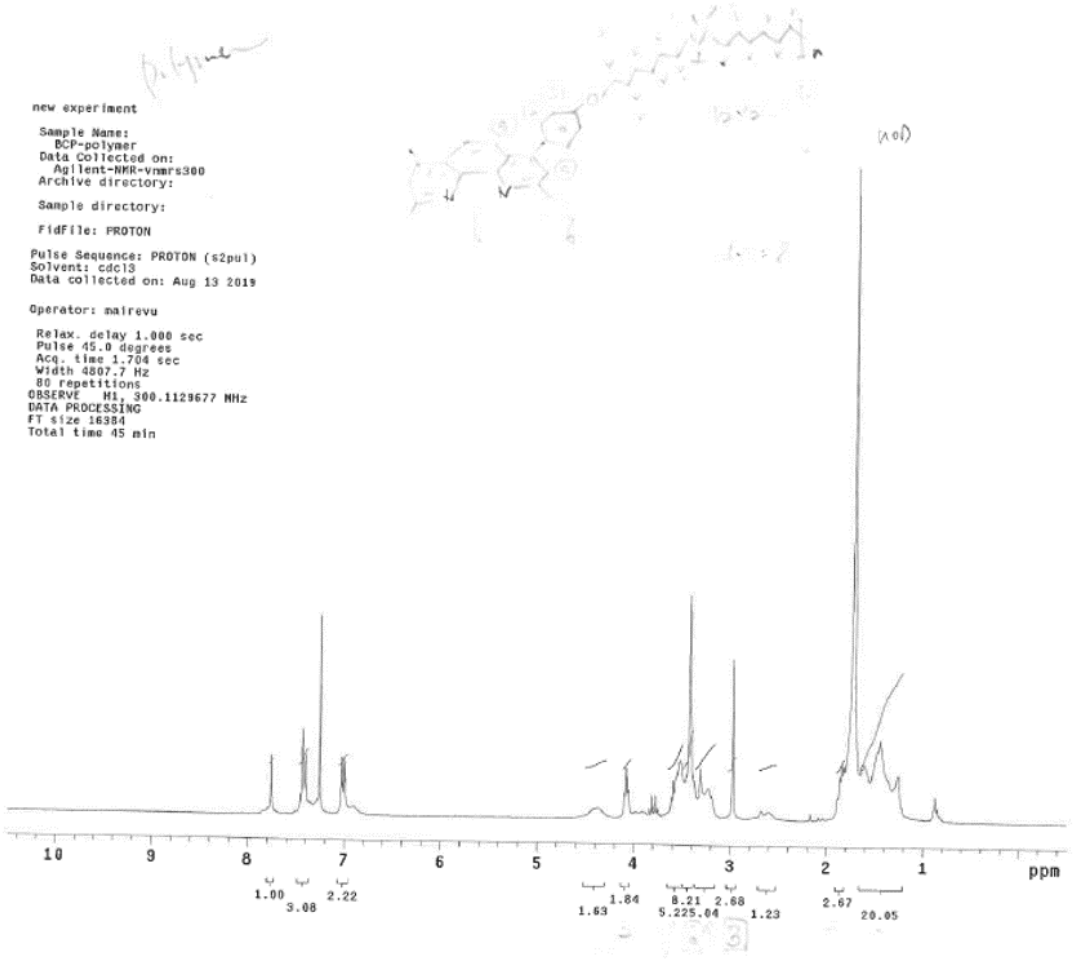

Figure S1. ^{1}H-NMR data for poly-BCP.

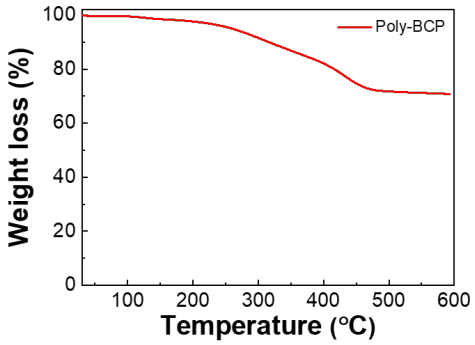

Figure S2. Thermogravimetric analysis of the polymer under N_2.

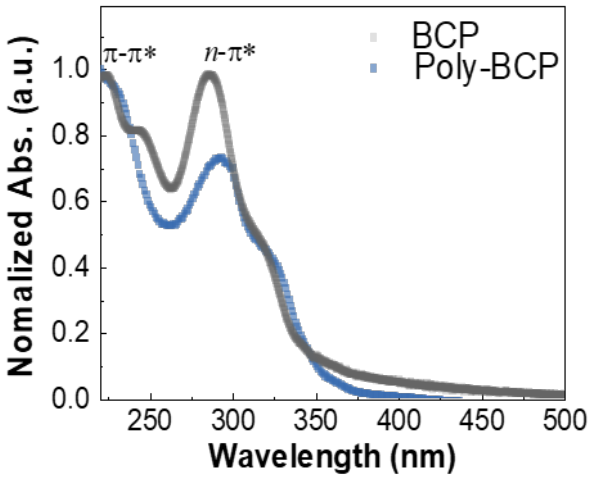

Figure S3. UV-Vis absorption spectra of BCP (black) and poly-BCP (blue) thin films.

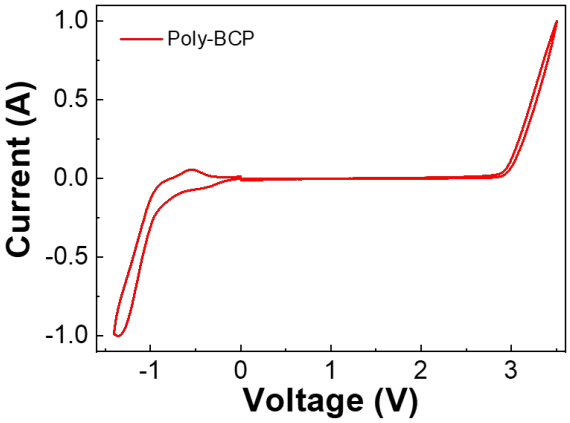

Figure S4. Cyclic voltammetry (CV) curve of the polymer in 0.1 M TBAP in acetonitrile solution at a scan rate of 100 $mV \cdot s^{-1}$ at room temperature (*vs* an Ag quasi-reference electrode).

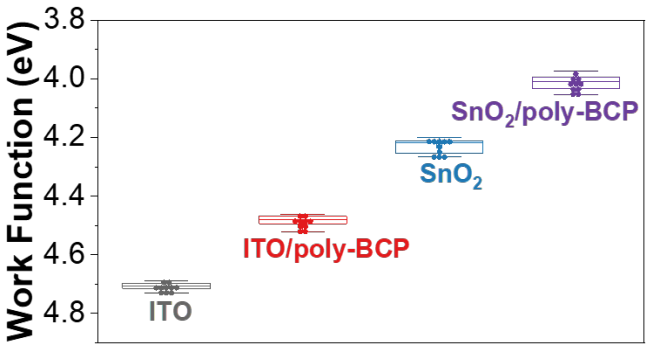

Figure S5. Work function (WF) of each film measured by a Kelvin probe: ITO (black), ITO/poly-BCP (red), SnO_2 (blue), and SnO_2/poly-BCP (purple).

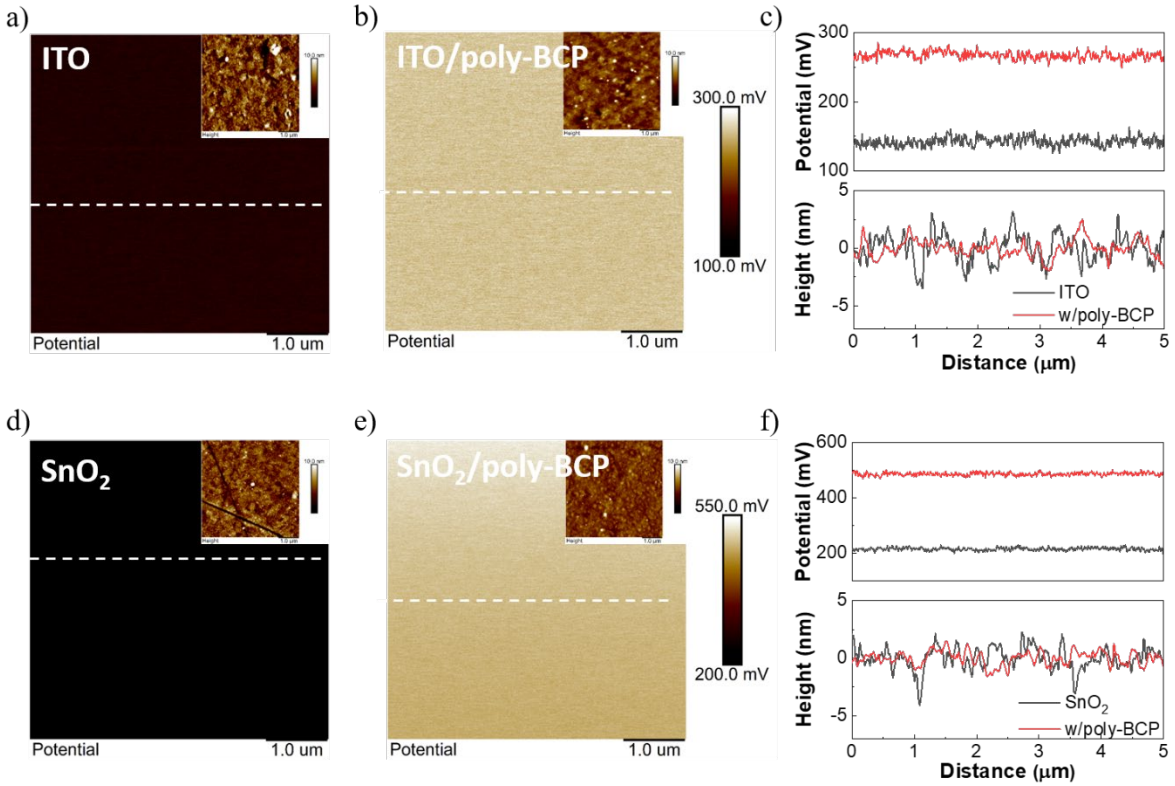

Figure S6. KPFM analysis of each film (AFM topology image are shown in the inset): ITO (a), ITO/poly-BCP (b), SnO_2 (d), and SnO_2 /poly-BCP (e). Extracted height and potential profiles of the corresponding films: ITO and ITO/poly-BCP film (c) and SnO_2 and SnO_2 /poly-BCP film (f).

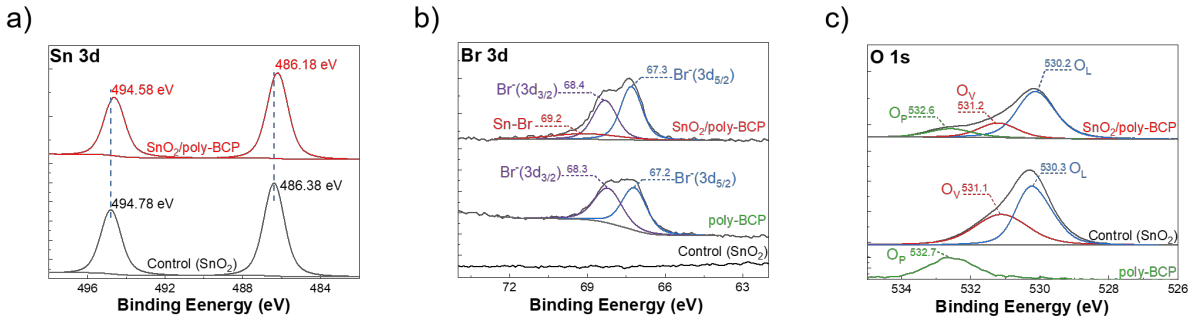

Figure S7. X-ray photoelectron spectra (XPS) of a) Sn 3d, b) Br 3d and c) O 1s peaks for each thin films.

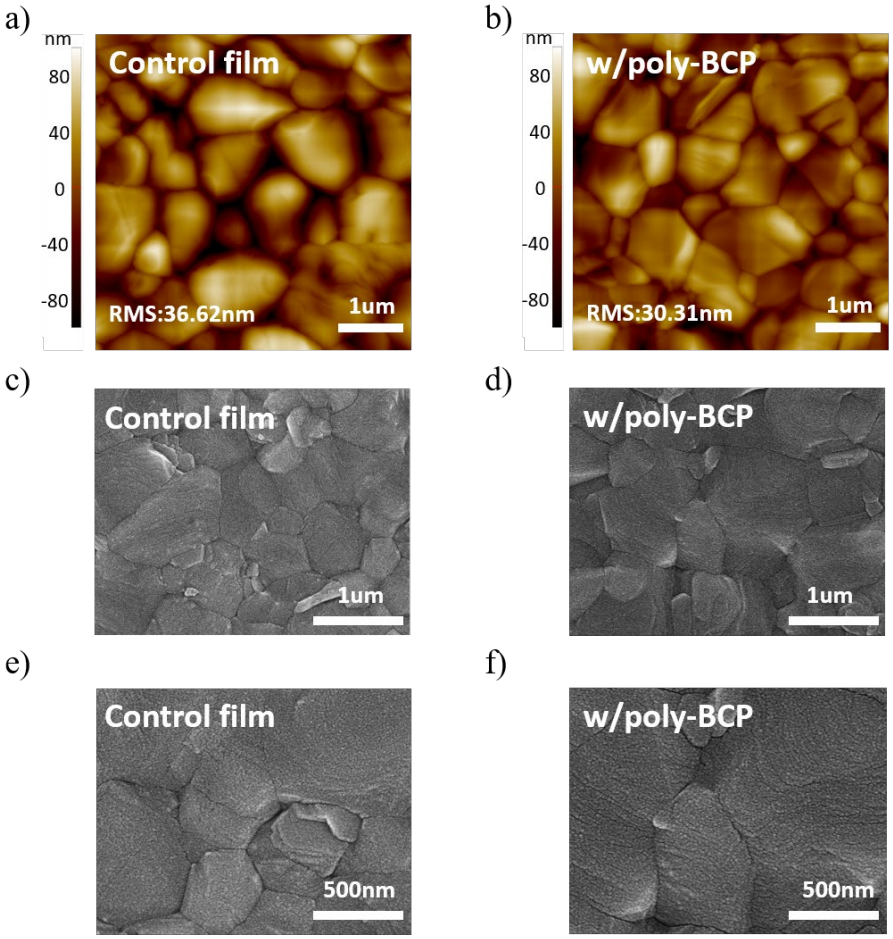

Figure S8. Surface analysis of each PVK film. AFM topology image of PVK films on a) SnO_2 (Control) and b) SnO_2/poly-BCP (w/ poly-BCP). SEM top view images of control PVK (c, e) and w/ poly-BCP (d, f).

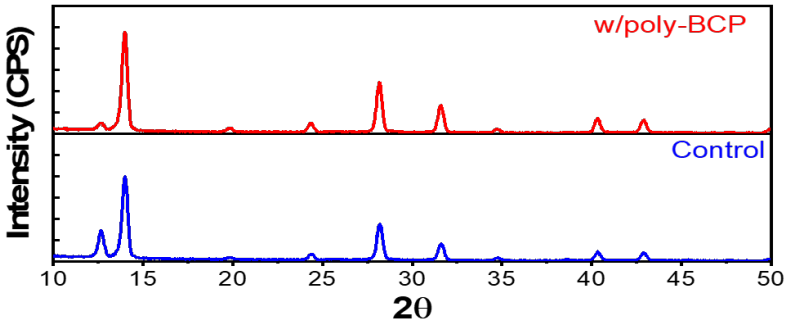

Figure S9. XRD analysis of PVK (blue) and w/poly-BCP PVK films (red).

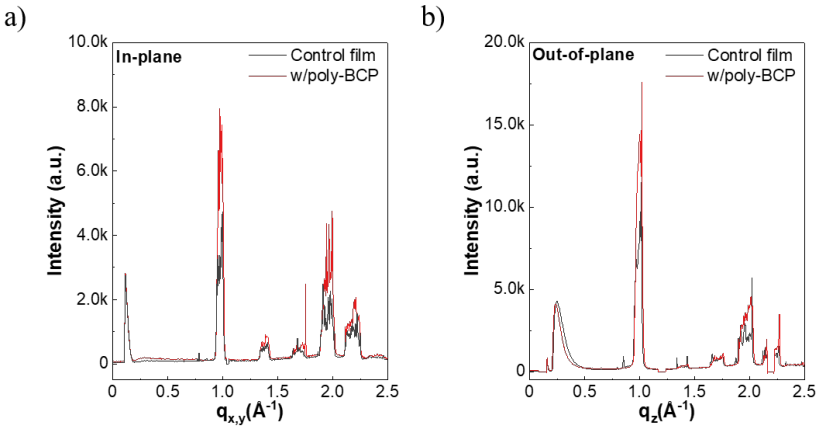

Figure S10. 1D GIWAXs plot for a) in-plane and b) out-of-plane directions in control (black) and with poly-BCP (red) PVK film.

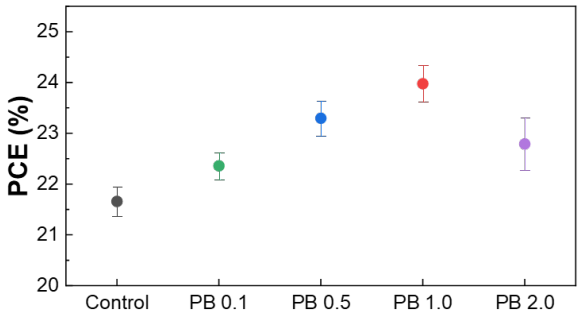

Figure S11. Dependence of device performance on the concentration of poly-BCP (PB) solution.

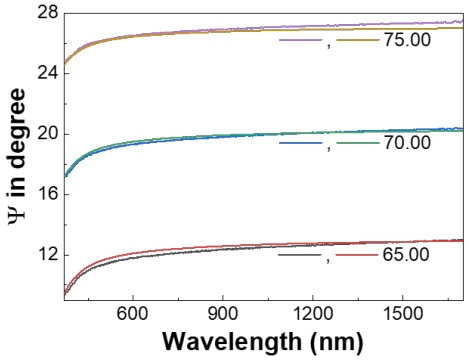

Figure S12. Ellipsometric parameters dependent on the incident angle of the optimized poly-BCP thin film (solution concentration:1mg/ml).

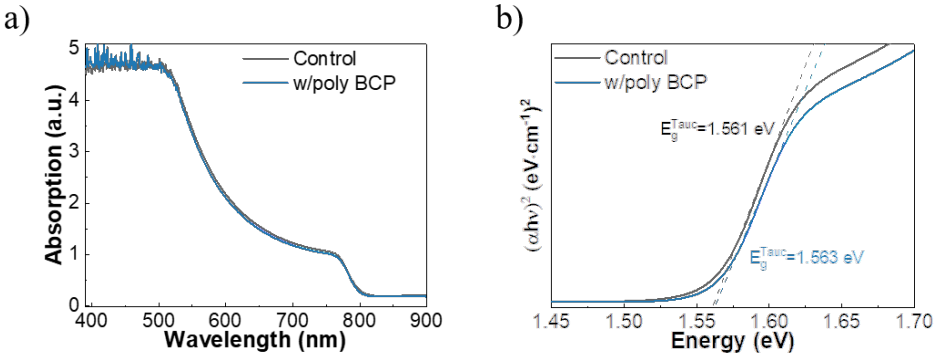

Figure S13. Bandgap analysis of PVK films. a) UV-Vis absorption spectrum of each film: control PVK film (black) and w/poly-BCP PVK film(blue). b) Corresponding Tauc plot based on the UV-Vis absorption spectrum.

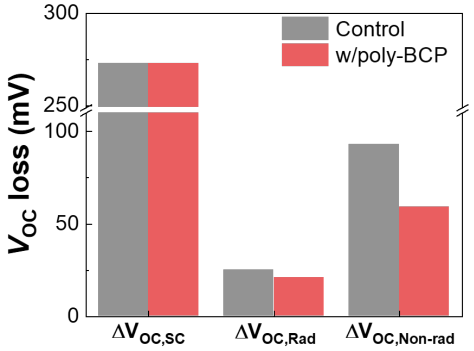

Figure S14. Histograms of radiative and nonradiative V_{OC} loss: control device (black) and w/poly-BCP device (red). The nonradiative V_{OC} loss is calculated using the function $\ln(EQE_{EL})kT/q$, wherein EQE_{EL}, k, T, and q are the electroluminescence external quantum efficiency, Boltzmann constant, Kelvin temperature, and elementary charge constant, respectively.

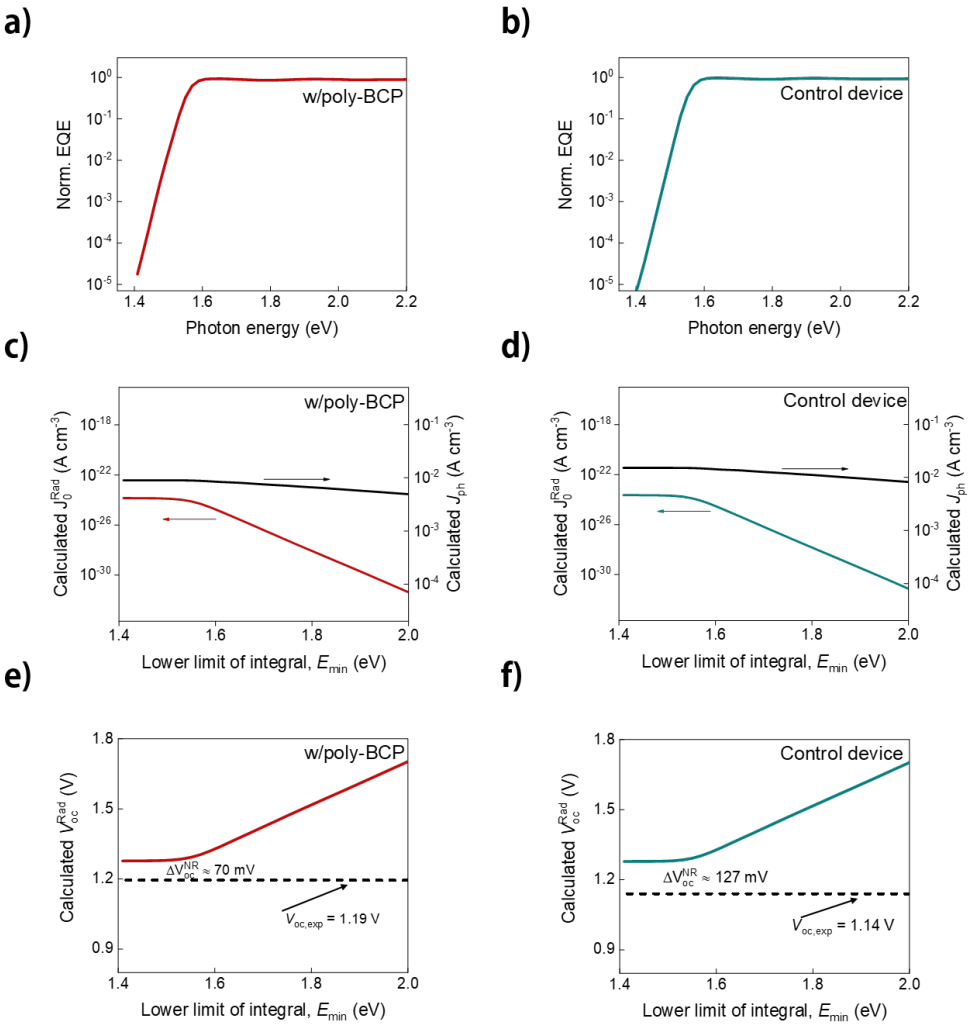

Figure S15. Normalized external quantum efficiency (EQE_{PV}) of a w\poly-BCP (left column) and as control (right column) device plotted as a function of photon energy. From the EQE_{PV} spectra, the dark saturation current density limit $\boldsymbol{J_0^{Rad}}$ and the photocurrent density $\boldsymbol{J_{Ph}}$ were calculated along $\boldsymbol{J_0^{Rad}(E_{min}) = q\int_{E_{min}}^{\infty} EQE_{PV}\Phi_{BB}\,dE}$ (where $\boldsymbol{\Phi_{BB}}$ denotes the black body spectrum at room temperature, $\boldsymbol{q}$ the elementary charge, $\boldsymbol{E}$ the photon energy, and $\boldsymbol{E}_{min}$ the lower limit of integral) and $\boldsymbol{J_{Ph}(E_{min}) = q\int_{E_{min}}^{\infty} EQE_{PV}\Phi_{sun}\,dE}$ (where $\boldsymbol{\Phi_{sun}}$ denotes the solar spectrum). (c,d) Calculated $\boldsymbol{J_0^{Rad}}$ (left axis; coloured line) and $\boldsymbol{J_{Ph}}$ (right axis; black line) plotted as a function of $\boldsymbol{E}_{min}$. The radiative open-circuit voltage ($\boldsymbol{V_{OC}^{Rad}}$) limit was calculated in accordance with $\boldsymbol{V_{OC}^{Rad} = \frac{kT}{q}\ln\left(\frac{J_{Ph}}{J_0^{Rad}} + 1\right)}$, where $\boldsymbol{k}$ is the Boltzmann constant and $\boldsymbol{T}$ the temperature. (e,f) Calculated $\boldsymbol{V_{OC}^{Rad}}$ (solid lines) for both devices plotted as a function of $\boldsymbol{E}_{min}$, and compared with the experimental $\boldsymbol{V}_{oc,exp}$ (dashed line), as obtained from current density *versus* applied voltage (*J-V*) characteristics under AM 1.5G conditions. Non-radiative voltage losses $\boldsymbol{\Delta V_{oc}^{NR} = V_{OC}^{Rad} - V_{oc,exp}}$ were found to be 70 mV and 127 mV for the w/poly-BCP and as control device, respectively.

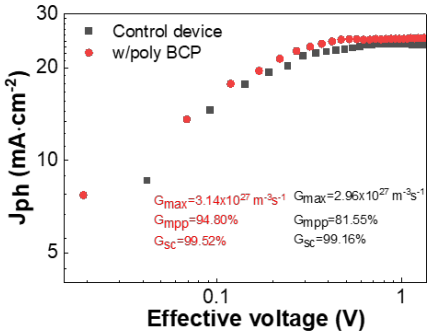

Figure S16. Effective voltage characterization of PSCs – control device (black) and with poly-BCP device (red).

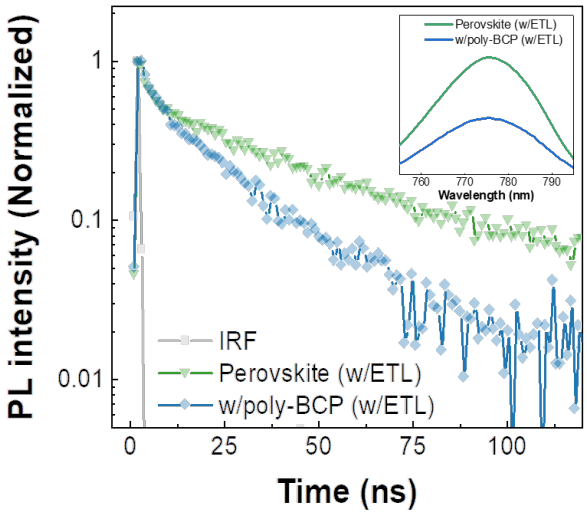

Figure S17. TRPL decay curves of control (green) and with poly-BCP (blue) PVK film with SnO_2 ETL samples. Related steady-state PL (inset).

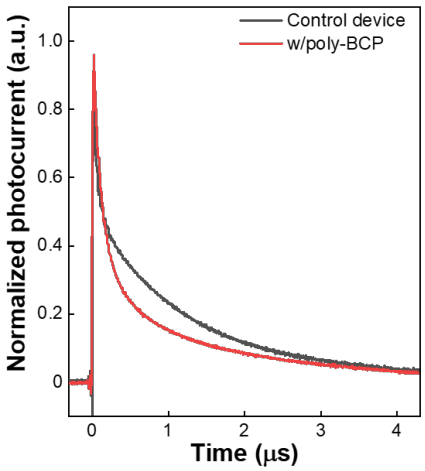

Figure S18. Transient photocurrent measurement – control device (black) and with poly-BCP device (red).

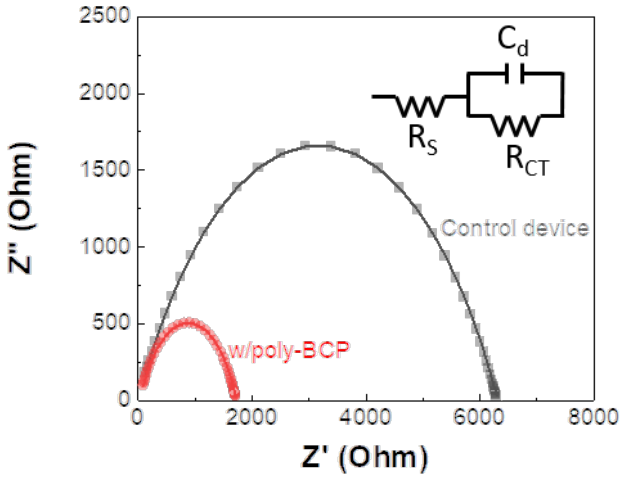

Figure S19. Nyquist plots of PSCs – control device (black) and with poly-BCP device (red). The corresponding equivalent circuit to fit the graphs (inset).

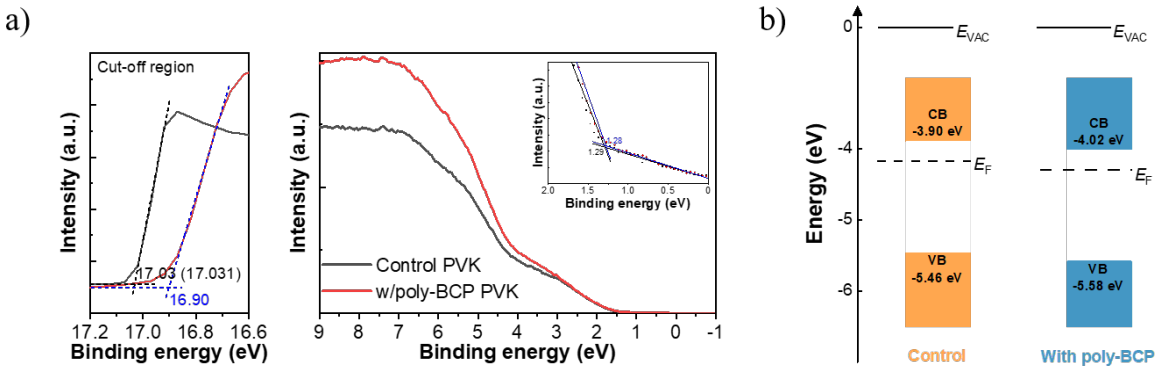

Figure S20. Energy-level characterization of each PVK film. a) UPS data for the control PVK film and w/poly-BCP PVK film: secondary electron cutoff region ($E_{cut\text{-}off}$, left), valance band (VB) region (right), and enlarged VB region (inset). b) Energy level scheme of the control PVK film (orange) and w/poly-BCP PVK film (blue) based on the parameters derived from the UPS spectra. The WF was calculated from following equation: $\boldsymbol{WF = 21.22 - E_{cut-off}}$, where 21.22 is the energy of the incident laser light (He).

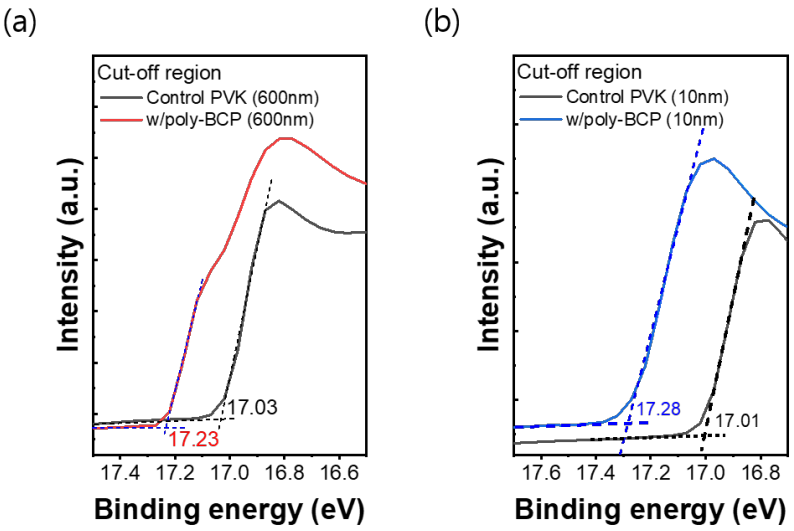

Figure S21. Secondary electron cut-off region of UPS analysis for thickness dependence of each PVK films; 600nm PVK films (a) and 10nm PVK films (b).

Table S1. Electrochemical potentials and energy levels of the polymer.

	optical band gap[a] (eV)	LUMO[b] (eV)	HOMO[b] (eV)	E_{ox}[c] (V)	E_{red}[c] (V)	electrochemical band gap[d] (eV)
Poly-BCP	3.50	-3.92	-7.75	2.95	-0.88	3.83

[a]The optical energy band gap was estimated from the onset wavelength of the optical absorption. [b]Calculated from the oxidation potentials. [b]Calculated from the reduction potentials. [c]Onset oxidation and reduction potential measured by cyclic voltammetry. [d]Calculated from the $E_{ox}$and E_{red}.

Table S2. Parameters for deconvolution of O 1s XPS spectra of each thin film.

Sample	**Binding Energy (eV)**	**Peak Area (counts)**	**Concentration (at. %)**	**Assignment**
SnO_2	530.3	249941.77	55.56	Sn-O-Sn (O_L)
	531.1	199896.84	44.43	Oxygen vacancies (O_V)
SnO_2/ poly-BCP	530.2	128425.14	66.34	O_L
	531.2	39608.63	20.46	O_V
	532.6	25547.70	13.20	Ether functional group (O_P)
Poly-BCP	532.7	28200.40	99.99	O_P

Table S3. Representative conventional n-i-p planar PSCs with SnO_2 electron transport layer.

	V_{OC}	PCE	Reference
1	1.14	22.40	[1]
2	1.16	21.43	[2]
3	1.21	21.75	[3]
4	1.18	22.21	[4]
5	1.17	23.10	[5]
6	1.11	21.73	[6]
7	1.18	23.32	[7]
8	1.25	23.06	[8]
9	1.21	23.38	[9]
10	1.16	23.20	[10]
11	1.15	21.63	[11]
12	1.18	24.01	[12]
13	1.18	24.63	[13]
14	1.14	22.77	[14]
15	1.19	22.42	[15]
16	1.18	22.36	[16]
17	1.17	23.68	[17]
18	1.17	23.09	[18]
19	1.16	23.92	[19]
20	1.19	25.40	[20]
21	1.22	21.09	[21]
22	1.21	24.43	This work

Table S4. PL decay parameters of each sample with SnO_2 electron transport layer.

Samples	Fitted time constants (ns)		
	τ_1	τ_2	τ_{avg} [a)]
SnO_2/perovskite	2.4 (55%)	50.8 (45%)	27.2
SnO_2/poly-BCP/perovskite	2.9 (51%)	24.2 (49%)	18.6

[a)] τ_{avg}: average decay time, all samples use quartz substrate.

Table S5. Electrochemical impedance spectroscopy (EIS) measurement of PSCs without and with a poly-BCP layer.

Samples	R_s[a] (Ω)	R_{ct}[b] (Ω)
Control	27.3	6.23×10^3
w/poly-BCP	31.2	1.69×10^3

[a] R_s: series resistance of the PSCs, [b] R_{ct}: charge transfer resistance of the PSCs. The values were

calculated by using the Randles circuit model at the junction with an electrolyte based on the EIS results.

Table S6. Parameters of the Fermi energy level for each thin film based on the UPS analysis.

Samples	E_{Fn}[a] (eV)	E_{Fp}[b] (eV)	V_{bi}[c] (eV)
Control	4.170	4.169	0.001
w/poly-BCP	3.970	4.300	0.330

[a] E_{Fn}: Fermi energy level of the n-type semiconductor (SnO_2 ETL in this work), [b] E_{Fp}: Fermi energy level of the p-type semiconductor (PVK thin film in this work). [c] V_{bi}: Built-in-potential at the interface between n-type semiconductor and p-type semiconductor ($V_{bi} = E_{Fp} - E_{Fn}$).

References

[1] L. Xiong, J. Li, F. Ye, H. Wang, Y. Guo, X. Ming, Q. Chen, S. Zhang, R. Xie, Z. Chen, Y. Lv, G. Hu, Y. He, G. Fang, Advanced Functional Materials 2021, 31.

[2] K. Choi, J. Lee, H. I. Kim, C. W. Park, G.-W. Kim, H. Choi, S. Park, S. A. Park, T. Park, Energy & Environmental Science 2018, 11, 3238.

[3] J. Ye, Y. Li, A. A. Medjahed, S. Pouget, D. Aldakov, Y. Liu, P. Reiss, Small 2021, 17, e2005671.

[4] F. Li, Z. Shen, Y. Weng, Q. Lou, C. Chen, L. Shen, W. Guo, G. Li, Advanced Functional Materials 2020, 30.

[5] H. Lu, Y. Liu, P. Ahlawat, A. Mishra, W. R. Tress, F. T. Eickemeyer, Y. Yang, F. Fu, Z. Wang, C. E. Avalos, B. I. Carlsen, A. Agarwalla, X. Zhang, X. Li, Y. Zhan, S. M. Zakeeruddin, L. Emsley, U. Rothlisberger, L. Zheng, A. Hagfeldt, M. Gratzel, Science 2020, 370.

[6] P. Huang, Q. Chen, K. Zhang, L. Yuan, Y. Zhou, B. Song, Y. Li, Journal of Materials Chemistry A 2019, 7, 6213.

[7] Q. Jiang, Y. Zhao, X. Zhang, X. Yang, Y. Chen, Z. Chu, Q. Ye, X. Li, Z. Yin, J. You, Nature Photonics 2019, 13, 460.

[8] Q. Lou, Y. Han, C. Liu, K. Zheng, J. Zhang, X. Chen, Q. Du, C. Chen, Z. Ge, Advanced Energy Materials 2021.

[9] J. Zhuang, P. Mao, Y. Luan, N. Chen, X. Cao, G. Niu, F. Jia, F. Wang, S. Cao, J. Wang, Advanced Functional Materials 2021, 31.

[10] E. H. Jung, B. Chen, K. Bertens, M. Vafaie, S. Teale, A. Proppe, Y. Hou, T. Zhu, C. Zheng, E. H. Sargent, ACS Energy Letters 2020, 5, 2796.

[11] H. Bi, X. Zuo, B. Liu, D. He, L. Bai, W. Wang, X. Li, Z. Xiao, K. Sun, Q. Song, Z.

Zang, J. Chen, Journal of Materials Chemistry A 2021, 9, 3940.

[12] R. Yuan, B. Cai, Y. Lv, X. Gao, J. Gu, Z. Fan, X. Liu, C. Yang, M. Liu, W.-H. Zhang, Energy & Environmental Science 2021, 14, 5074.

[13] Y.-W. Jang, S. Lee, K. M. Yeom, K. Jeong, K. Choi, M. Choi, J. H. Noh, Nature Energy 2021, 6, 63.

[14] W. Hui, Y. Yang, Q. Xu, H. Gu, S. Feng, Z. Su, M. Zhang, J. Wang, X. Li, J. Fang, F. Xia, Y. Xia, Y. Chen, X. Gao, W. Huang, Adv Mater 2020, 32, e1906374.

[15] S. Xiong, Z. Hou, W. Dong, D. Li, J. Yang, R. Bai, Y. Wu, D. Li, H. Wu, Z. Ma, J. Xu, X. Liu, Q. Bao, Advanced Energy Materials 2021, 11.

[16] M. Guo, J. Bo, X. Chen, P. Wan, M. Chen, Q. Li, C. Luo, Y. Chen, S. Chen, Advanced Energy Materials 2021, 11.

[17] S. You, H. Zeng, Z. Ku, X. Wang, Z. Wang, Y. Rong, Y. Zhao, X. Zheng, L. Luo, L. Li, S. Zhang, M. Li, X. Gao, X. Li, Adv Mater 2020, 32, e2003990.

[18] P. Hang, J. Xie, C. Kan, B. Li, Y. Zhang, P. Gao, D. Yang, X. Yu, Adv Mater 2021, 33, e2006910.

[19] H. Zai, J. Su, C. Zhu, Y. Chen, Y. Ma, P. Zhang, S. Ma, X. Zhang, H. Xie, R. Fan, Z. Huang, N. Li, Y. Zhang, Y. Li, Y. Bai, Z. Gao, X. Wang, J. Hong, K. Sun, J. Chang, H. Zhou, Q. Chen, Joule 2021, 5, 2148.

[20] J. J. Yoo, G. Seo, M. R. Chua, T. G. Park, Y. Lu, F. Rotermund, Y. K. Kim, C. S. Moon, N. J. Jeon, J. P. Correa-Baena, V. Bulovic, S. S. Shin, M. G. Bawendi, J. Seo, Nature 2021, 590, 587.

[21] M. Singh, A. Ng, Z. Ren, H. Hu, H.-C. Lin, C.-W. Chu, G. Li, Nano Energy 2019, 60, 275.